

Enhancing streamflow forecast and extracting insights using long-short term memory networks with data integration at continental scales

Dapeng Feng, Kuai Fang, and Chaopeng Shen¹

Civil and Environmental Engineering
Pennsylvania State University

Abstract

Recent observations with varied schedules and types (moving average, snapshot, or regularly spaced) can help to improve streamflow forecast but it is difficult to effectively integrate them. Based on a long short-term memory (LSTM) streamflow model, we tested different formulations in a flexible method we call data integration (DI) to integrate recently discharge measurements to improve forecast. DI accepts lagged inputs either directly or through a convolutional neural network (CNN) unit. DI can ubiquitously elevate streamflow forecast performance to unseen levels, reaching a continental-scale median Nash-Sutcliffe coefficient of 0.86. Integrating moving-average discharge, discharge from a few days ago, or even average discharge of the last calendar month could all improve daily forecast. It turned out, directly using lagged observations as inputs was comparable in performance to using the CNN unit. Importantly, we obtained valuable insights regarding hydrologic processes impacting LSTM and DI performance. Before applying DI, the original LSTM worked well in mountainous regions and snow-dominated regions, but less so in regions with low discharge volumes (due to either low precipitation or high precipitation-energy synchronicity) and large inter-annual storage variability. DI was most beneficial in regions with high flow autocorrelation: it greatly reduced baseflow bias in groundwater-dominated western basins; it also improved the peaks for basins with dynamical surface water storage, e.g., the Prairie Potholes or Great Lakes regions. However, even DI cannot help high-aridity basins with one-day flash peaks. There is much promise with a deep-learning-based forecast paradigm due to its performance, automation, efficiency, and flexibility.

Key points

1. We propose an LSTM network with flexible data integration (DI), which can use various types of observations to improve discharge forecast.
2. Adding a convolutional neural network unit can reduce overfitting but cannot outperform directly accepting lagged discharge as inputs.
3. DI benefits are strong in regions with high flow autocorrelation, due to either groundwater dominance or surface water storage.

¹ Corresponding author: cshen@engr.psu.edu
This paper is currently under second review at a journal.

1. Introduction

Flooding is the biggest weather-related killer in the U.S. (NWS, 2014), while droughts incur on average \$6B damage a year in the U.S. (NOAA, 2016). As the climate is predicted to bring more frequent extreme events for many parts of the U.S. (Hirsch & Archfield, 2015; Stocker et al., 2013), accurate predictions of their outcomes are of not only scientific value but also great societal significance. In the US, hydrologic models such as the conceptual Sacramento Soil Moisture Accounting (SAC-SMA) model (Anderson & McDonnell, 2005), among others (Krajewski et al., 2017; Maidment, 2017), have played major roles in supporting operational streamflow forecast. These models have been extensively calibrated and tested over the US.

In the realm of process-based hydrologic modeling, the common tool of utilizing observations to improve short-term streamflow forecast at large scales is data assimilation (DA) (Clark et al., 2008; Houser et al., 1998; Vrugt et al., 2006). The main objectives of DA are to absorb recent observations to update model internal states, to better forecast future variables including observed and unobserved variables, and, less frequently, to update model structures or parameter sets. DA works by establishing the covariance between the internal states of a process-based model and observed variables and using the difference between the observation and the model-simulated variable(s) to update the model internal states. Some variants of the DA algorithm can also help to correct model structure equations given some prior information (Bulygina et al., 2012; Nearing & Gupta, 2015). The uncertainty of the observation is considered through the covariance matrix. With the injection of new data, DA can remove autocorrelated effects of inevitable forcing errors and steer the model from incorrect trajectories (due to inadequate model structure or parameters).

Recently, time-series deep learning (DL) has emerged as a powerful and versatile modeling tool in hydrology (Fang et al., 2017; Kratzert et al., 2018; Shen, 2018; Shen et al., 2018), but few studies have examined streamflow forecast with DL, especially at large scales. DL models learn response patterns from the massive amount of data directly, without requiring manually designed features or making strong

structural assumptions (LeCun et al., 2015; Schmidhuber, 2015), and is hence less influenced by model structural errors. Our earlier work showed that the long short-term memory (LSTM) network (Hochreiter & Schmidhuber, 1997), can effectively learn soil moisture dynamics from satellite-based soil moisture products (Fang et al., 2017) and reproduce multi-year trends for root-zone soil moisture (Fang et al., 2018), with superior performance than simpler statistical methods. Since then, LSTM has already been utilized in a number of prediction tasks, e.g., lake water temperature (Jia et al., 2019), water table depth (Zhang et al., 2018), among others. Especially, a number of studies predicted streamflow using LSTM (Hu et al., 2018; Kratzert et al., 2018; Kratzert, Klotz, et al., 2019; Le et al., 2019; Sudriani et al., 2019). Most of these applications tend to focus on a few basins for their respective case studies, while Kratzert et al., (2018, 2019) utilized Catchment Attributes and Meteorology for Large-Sample Studies (CAMELS), a dataset with more than six hundred relatively undisturbed basins (Addor et al., 2017; Newman et al., 2014). While progress is being made, these studies appear to only scratch the surface of what could be achieved by time series DL. In particular, there is significant potential in leveraging DL to flexibly absorb recent observations, whose value was not exploited to the greatest extent.

LSTM has often used lagged observations as inputs. For example, in the task of sentence completion, a partial sentence is provided as input to predict the next word, and, when the new word is known, it is appended to the input sentence to predict the next word. Similarly, to predict streamflow at one gage, Hu et al., (2018) and Le et al., (2018) inserted streamflow observations an hour or a day before the prediction to forecast tasks and showed promising results from LSTM. However, both of these streamflow studies trained the model on one gage without descriptors for the basin. While useful for the training basin, these models are not transferable to regions outside of the training one, and thus cannot learn from large-scale datasets. Consequently, a locally-trained model cannot help to derive hydrologic insights that depend on contrasting and learning from regional patterns and their gradients. On the flip side, because landscape parameters alter streamflow responses, it is an open question whether a uniform model could be trained to high performance for integrating recent observations at the CONUS scale.

If the observations are the most recent streamflow records, e.g., from yesterday, the forecast task is effectively predicting the daily streamflow changes due to various hydrologic processes that occur during the day, e.g., recession, new runoff, or baseflow return from early season recharge. The problem is arguably much simpler compared to the projection problem, which requires long-term memory and could be influenced by the accumulated errors. Given this problem scope, it is not clear how advantageous LSTM would be compared to simpler methods such as the autoregressive model (AR) with exogenous terms, as AR was already successful at modeling recession and daily runoff processes (Vogel & Kroll, 1996).

Many sources of data, with various observational schedules (different revisit times and average vs. snapshot measurement types), are relevant to improving streamflow forecast. For example, some hydrologic stations in and outside of US report discharge only on weekly or monthly time intervals (Wang et al., 2009); The planned Surface and Water Ocean Topography (SWOT) mission will have recurrent snapshot measurements of around 11 days (Biancamaria et al., 2016). Operational constraints may often increase the latency between data acquisition and delivery. Furthermore, there are monthly-averaged satellite-based terrestrial water storage anomalies (TWSA) (Swenson, 2012) or soil moisture observations (snapshots), which are available on a 2-to-3-day revisit schedule (Entekhabi, 2010). The assimilation of data with various types, time scale, and latency through traditional DA entails substantial expert supervision in selecting the most appropriate assimilation, data transformation (Clark et al., 2008), and bias correction schemes. Especially since models often exhibit different behaviors from the observations, DA procedures often need bias correction to avoid distorting model internal states (Farmer et al., 2018). With hydrologic datasets, it has not been established whether LSTM can effectively utilize observations of these data with different types (multi-day-averages vs. single-day), latency, and intervals (daily vs. weekly or monthly, etc).

In this work, we tested an efficient and flexible LSTM-based method that automatically assimilates observations of various types to improve the forecasts. We compared two versions of this method which we call data integration (DI): one directly accepts lagged observations among the inputs, while the other passes a segment of recent observations through a convolutional neural network (CNN) unit. The use of

“DI” does not imply an entirely new method, but it is meant for easier referencing and differentiation from DA which is often used in forecast tasks. DI does not utilize a pre-calibrated system dynamic model as DA does. Rather, the method integrates the data injection and prediction steps into one. Of the abovementioned objectives of DA, DI alters the internal states of LSTM and improves the prediction of future predicted variables, but does not predict unobserved variables. We hope to address the following questions: (1) *Does LSTM with DI outperform reference statistical models for the forecast problem?* (2) *Can LSTM flexibly and effectively utilize time-lagged, moving average, and regularly-spaced streamflow with different latencies for forecast?* (3) *Where does LSTM perform poorly with or without DI and what are the hydrologic processes behind such patterns?* In the following, we first describe the datasets, network and the DI method, and demonstrate the effectiveness of DI in comparisons to hydrologic models, simpler statistical models, and LSTM without DI. We then show how LSTM was able to integrate different types of data. Finally, we interpret where and why LSTM with or without DI delivers strong or poor performance and relate that to hydrologic processes. We show that besides making improved estimates, big data machine learning could provide insights into how hydrologic systems function differently across the landscape.

2. Data and Methods

2.1 Camels data

We used the CAMELS dataset (Addor et al., 2017; Newman et al., 2014), which consists of the basin averaged hydrometeorological time series, catchment attributes, and streamflow observations from USGS for 671 catchments over the Continental US (CONUS). These basins were selected with minimum human disturbances. Most of the daily streamflow observations in CAMELS start from 1980 and end in 2014. The forcing data we used in this study is NLDAS daily data. The CAMELS catchment attributes include topography, climate characteristics, hydrological signatures, land cover, soil, and geology characteristics, and are also inputs to our LSTM model (Table 1). Compared to another effort (Kratzert et al., 2019), we did not employ mean climate attributes as predictors, as we wish to see a strong model can be trained using only physiographical attributes. We present most of our results using all of the 671 catchments in CAMELS. Previous studies have noted either unclear watershed boundaries or too-large watershed areas with 140

basins excluded from evaluations (Newman et al., 2017). Thus, we also report results from this subset (531 basins) for the sake of comparison.

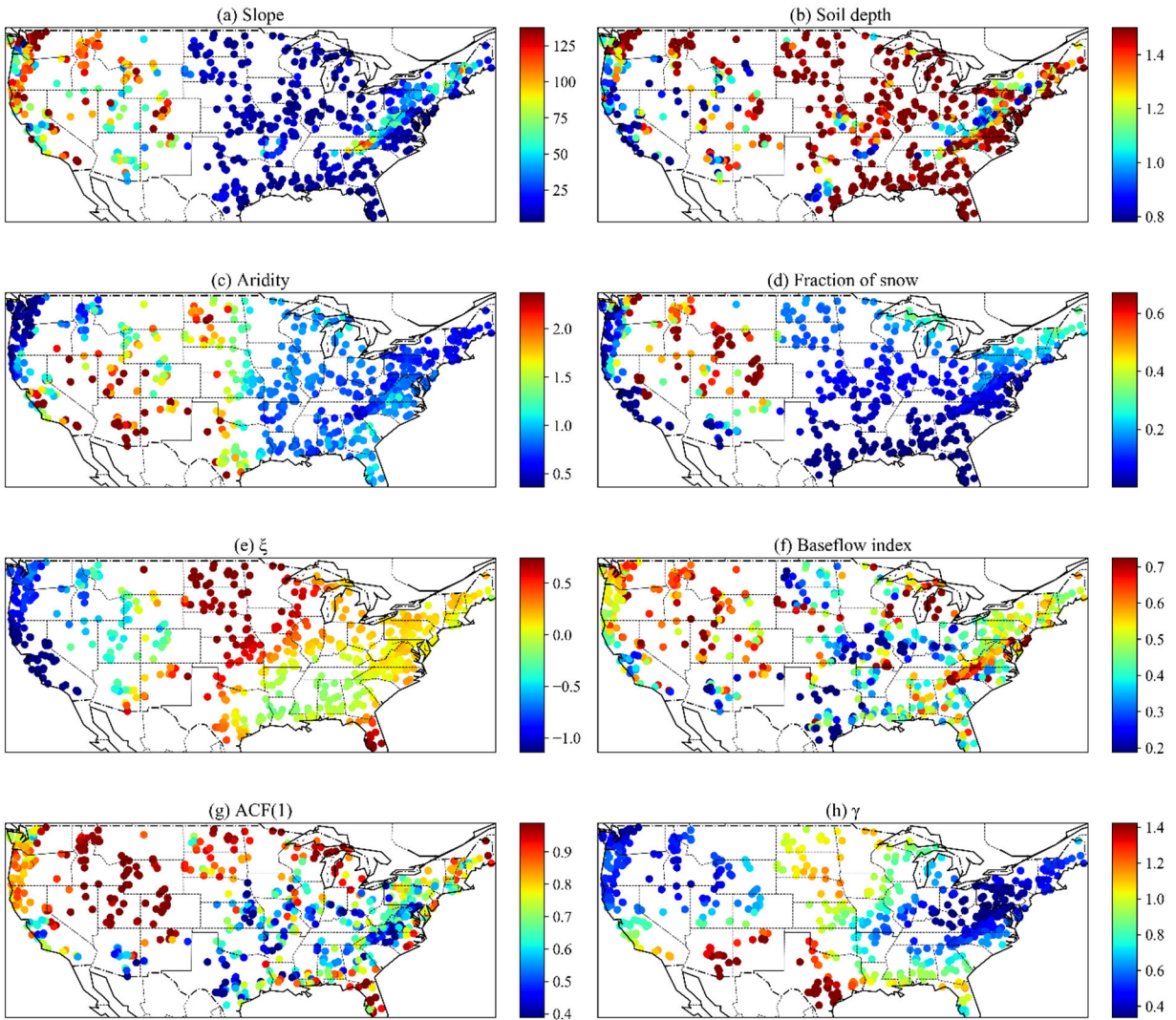


Figure 1. The characteristics of CAMELS basins. (a) Slope: basin mean slope; (b) Soil depth; (c) Aridity: ratio between annual potential evapotranspiration and precipitation; (d) Fraction of snow: fraction of precipitation falling as snow; (e) ξ : precipitation seasonality index which indicates how much precipitation and temperature are in phase; (f) Baseflow index; (g) ACF(1): 1-day-lag autocorrelation function of streamflow; (h) γ : the ratio of TWSA inter-annual and intra-annual variability.

Figure 1 plots eight attributes of the CAMELS basins, including mean slope, soil depth, aridity (ratio between annual potential evapotranspiration and precipitation), fraction of precipitation falling as snow (Fraction of snow), precipitation seasonality (ξ , explained below), fraction of basin outflow attributed to baseflow (baseflow index), 1-day-lag autocorrelation function of streamflow (ACF(1)), and the terrestrial water storage anomalies (TWSA) inter-annual variability (γ). ξ characterizes how much precipitation is seasonally in phase with energy inputs (Fang et al., 2016; Milly, 1994; Woods, 2009). It is positive when precipitation and energy are in phase, i.e., rainfall maximum occurs in the summer; it is close to 0 when rainfall is evenly distributed and negative when precipitation and potential evapotranspiration are completely opposite in phase, i.e., most precipitation is in the form of winter snow. γ is the ratio of variance explained by inter-annual variability and intra-annual variability for the TWSA provided by the Gravity Recovery and Climate Experiment (GRACE) mission, and higher values represent the basin water storage has high inter-annual variability compared to intra-annual. Baseflow index is the fraction of streamflow determined as baseflow via recession analysis (Ladson et al., 2013). Among these, slope and soil depths are closely related as mountains tend to have shallower soils. ξ is a climatic index while the baseflow index, ACF, can be seen as hydrologic signatures.

2.2. The LSTM model with data integration

We developed the LSTM streamflow model based on our previous soil moisture prediction work (Fang et al., 2017; 2018). LSTM is a type of recurrent neural network which learns from sequential data. Different from the simple recurrent networks with one state variable, LSTM added units such as “cell states” and “gates” (Hochreiter & Schmidhuber, 1997). These additions solved the vanishing gradient problem. The input, forget and output gates, which control what information to allow in, what to forget, and what to output, respectively, are all trained automatically and simultaneously, using input data to predict the target variable. This workflow is called “end-to-end” training, which avoids the need for expert-designed features. The memory cell enables LSTM to learn long-term dependencies such as snow and subsurface storages,

which are needed for streamflow predictions. Figure 2a illustrates the mechanism within an LSTM cell and the forward pass is described by the following equations:

$$\text{Input node: } \mathbf{g}^t = \tanh(\mathcal{D}(\mathbf{W}_{gx}\mathbf{x}^t) + \mathcal{D}(\mathbf{W}_{gh}\mathbf{h}^{t-1}) + \mathbf{b}_g) \quad (1)$$

$$\text{Input gate: } \mathbf{i}^t = \sigma(\mathcal{D}(\mathbf{W}_{ix}\mathbf{x}^t) + \mathcal{D}(\mathbf{W}_{ih}\mathbf{h}^{t-1}) + \mathbf{b}_i) \quad (2)$$

$$\text{Forget gate: } \mathbf{f}^t = \sigma(\mathcal{D}(\mathbf{W}_{fx}\mathbf{x}^t) + \mathcal{D}(\mathbf{W}_{fh}\mathbf{h}^{t-1}) + \mathbf{b}_f) \quad (3)$$

$$\text{Output gate: } \mathbf{o}^t = \sigma(\mathcal{D}(\mathbf{W}_{ox}\mathbf{x}^t) + \mathcal{D}(\mathbf{W}_{oh}\mathbf{h}^{t-1}) + \mathbf{b}_o) \quad (4)$$

$$\text{Cell state: } \mathbf{s}^t = \mathbf{g}^t \odot \mathbf{i}^t + \mathbf{s}^{t-1} \odot \mathbf{f}^t \quad (5)$$

$$\text{Hidden state: } \mathbf{h}^t = \tanh(\mathbf{s}^t) \odot \mathbf{o}^t \quad (6)$$

$$\text{Output: } \mathbf{y}^t = \mathbf{W}_{hy}\mathbf{h}^t + \mathbf{b}_y \quad (7)$$

where the superscript t is the time step, \mathbf{x} is the input vector to the LSTM cell, \mathcal{D} is the dropout operator, \mathbf{W} 's and \mathbf{b} 's are the network weights and bias parameters, respectively, σ is the sigmoidal function, \odot is element-wise multiplication operator, \mathbf{g} is the value after the input node, \mathbf{i} , \mathbf{f} , \mathbf{o} are the values of input, forget and output gates, respectively, \mathbf{h} is the hidden states, \mathbf{s} is the memory cell states, and \mathbf{y} is the predicted outputs. We implemented a fast and flexible LSTM code that can utilize the highly-optimized cudnn library from the PyTorch deep learning platform. We did not apply a dropout to \mathbf{g} in equation (4) as we did in previous work, as it is not well supported by cudnn.

Originally, the input of the original LSTM model includes the forcing and static attributes at the present time step. We call the model without DI the ‘‘projection model’’. For the forecast model, the original inputs are combined with recent observations to predict the output for the current time step. The data injection can occur by directly supplying part of the lagged observations as input to the LSTM or passing them through an operator that performs dimension reduction, or both:

$$\mathbf{I}^{(t)} = [\mathbf{x}_o^{(t)}, \mathbf{y}_{p1}^*] \quad (8)$$

$$\mathbf{x}^{(t)} = [\mathbf{ReLU}(W_I I^{(t)} + \mathbf{b}_I), \mathbf{g}(y_{p2}^*)] \quad (9)$$

where $\mathbf{x}_o^{(t)}$ is the original LSTM inputs including forcing and static attributes, y_{p1}^* is the part of recently available observations that is directly assimilated as inputs, and y_{p2}^* is the optional part of the observation that will go through further transformation represented by the dimensional-reduction operator \mathbf{g} , $\mathbf{x}^{(t)}$ is the final inputs into the LSTM unit in equation 1, and ReLU is the Rectified Linear Unit.

The network was trained on sequences of 365 days of 6 meteorological features and 17 static features (detailed in Table 1) to predict the discharge at each time step. This fashion of training is sometimes referred to as “sequence to sequence). For the forecast model, discharge observations are integrated into the model at every timestep following equation 8 & 9. At each time step, only observed discharges before this time were used with DI.

We can flexibility choose the subset of data to use as y_{p1}^* or y_{p2}^* and they are collectively referred to as y^* . If the optional \mathbf{g} operator is not used, DI amounts to using lagged discharges as inputs (Figure 2c). For \mathbf{g} , we tested passing a long set of historical record of streamflow as y_{p2}^* into a one-dimension (1D) CNN unit. The 1D CNN can accept a large number of inputs and reduce them to a small number of hidden layer outputs, which are subsequently fed into the LSTM (Figure 2c). The network is called a CNN-LSTM network. The rationale of introducing this unit is that CNN can extract important features such as recession rates or temporal gradients from dataset and reduce the number of weights, thus suppressing overfitting (see a small overview in Section 2.3 of the open-access article Shen, 2018). If we attempt to integrate long records of past observation directly through LSTM, the number of weight parameters in the input linear layer (W_I in Equation 9) increases with the number of inputs. Then, the fully-connected layer becomes large, which is generally unfavorable as such layers are prone to overfitting. We hypothesized that the network with the 1D-CNN unit would give the model more robust performance than directly sending all observations to LSTM. We use CNN-DI(p_1, p_1+p_2) to denote a network that accepts p_1 -day observations directly to LSTM’s input node and p_2 days of additional observations into the CNN units. In this paper, p_1+p_2 ranged

from 100 to 365 and the CNN coarsens the inputs to a hidden layer with a width of 3 to 10, respectively.

The configuration of the CNN unit is described in Table A1 in the Appendix.

The input term y^* ideally should have a steady meaning across time steps so the network can robustly learn its connection to the forecast target. Missing values very occasionally exist in y^* but present neural networks cannot handle NaN values. We also cannot interpolate because it would leak information from the future. Several alternative treatments exist for missing values in y^* . First, one could modify the forward function in the neural network to make predictions for the next time step, and then replace that value only when observations exist. This method could handle highly irregular and frequent missing values, but is computationally less efficient because it cannot utilize highly optimized computational libraries. Second, one could fill in a special value such as -99 which attempts to inform LSTM that this data point is missing, but the effects are hard to guarantee. Third, one could initially train a gap-filling network by using zeros to fill the missing data as described above and then use the resulting network to make predictions to fill the gaps and train a new DI network. In theory, this procedure can be iterated a few times until the network converges. In practice, the streamflow data have very few isolated missing data (there are indeed whole periods with no discharge data, which is simply avoided by the loss function). We tested all of these methods and found that the treatment scheme had little impact on the model predictions for this dataset. Hence, we used the approach of filling zeros, which is the easiest and fastest.

Table 1. Summary of the forcing and attribute variables used as inputs to the LSTM model

	Variable Name	Description	Unit
Forcing	PRCP	Precipitation	mm/day
	SRAD	Solar radiation	W/m ²
	Tmax	Maximum temperature	°C
	Tmin	Minimum temperature	°C
	Vp	Vapor pressure	Pa
	Dayl	Day length	s
Attributes	elev_mean	Catchment mean elevation	m
	slope_mean	Catchment mean slope	m/km
	area_gages2	Catchment area (GAGESII estimate)	km ²
	frac_forest	Forest fraction	-
	lai_max	Maximum monthly mean of the leaf area index	-
	lai_diff	Difference between the maximum and minimum monthly mean of the leaf area index	-
	dom_land_cover_frac	Fraction of the catchment area associated with the dominant land cover	-
	dom_land_cover	Dominant land cover type	-
	root_depth_50	Root depth at percentiles 50 extracted from a root depth distribution based on igbp land cover	m
	soil_depth_statgso	Soil depth	m
	soil_porosity	Volumetric porosity	-
	soil_conductivity	Saturated hydraulic conductivity	cm/hr
	max_water_content	Maximum water content	m
	geol_class_1st	Most common geologic class in the catchment	-
geol_class_2nd	Second most common geologic class in the catchment	-	
geol_porosity	Subsurface porosity	-	
geol_permeability	Subsurface permeability	m ²	

The directly integrated observation \mathbf{y}_{p1}^* can be of different types in our method because, given different types of observations, the network will adaptively discover the mathematical relationships between these observations and the prediction task. To test the hypothetical scenarios where different types of data are available, we tested integrating the following observation types: (1) a single daily observation that was acquired N days before the forecast, noted as DI(N), (2) the moving average of the previous N days' observations, noted as DI(N)-M, (3) the data that are averages of regular intervals on a fixed observational schedule, noted as DI(N)-R; and (4) all the observations of the previous N days, noted as DI(N)-A. For example, DI(1) means integrating the observations on the yesterday to improve the forecast for today; DI(3)-M means using the moving average value of the observations on the previous three days; DI(30)-R means integrating the regularly-spaced monthly mean observation of the last month. Then, when we are making daily predictions in the full month of July using DI(30)-R, \mathbf{y}^* will be the average streamflow of June. Lastly, the DI(3)-A concatenates three additional input items that are y_{t-1}^* , y_{t-2}^* , and y_{t-3}^* , respectively, when making a forecast for time step t .

The proposed model was trained from October 1, 1985 to September 30, 1995 and tested from October 1, 1995 to September 30, 2005. The loss function was set as the root mean squared error (RMSE) between the predicted streamflow and the USGS observations, and the Adadelta algorithm (Zeiler, 2012) was used as the optimization method. We manually tested hyperparameter combinations and used a mini-batch size of 100, a hidden-state size of 256, and a training-instance length of 365 days as indicated in Table A1 in the Appendix. This length was substantially longer than our previous soil moisture prediction case in (Fang et al., 2017) where lengths of 30 or 60 days were used. The longer length here can represent catchment snow and subsurface storage processes that have longer-term memory compared to surface soil moisture. It needs to be noted that this length does not limit the memory of LSTM to 365 days. We did not invoke any automatic optimization schemes to tune them for the sake of simplicity. Considering the stochastic nature of the training procedure, we employed an ensemble of six simulations with different random seeds for each DI experiment. The ensemble-averaged discharge was also evaluated.

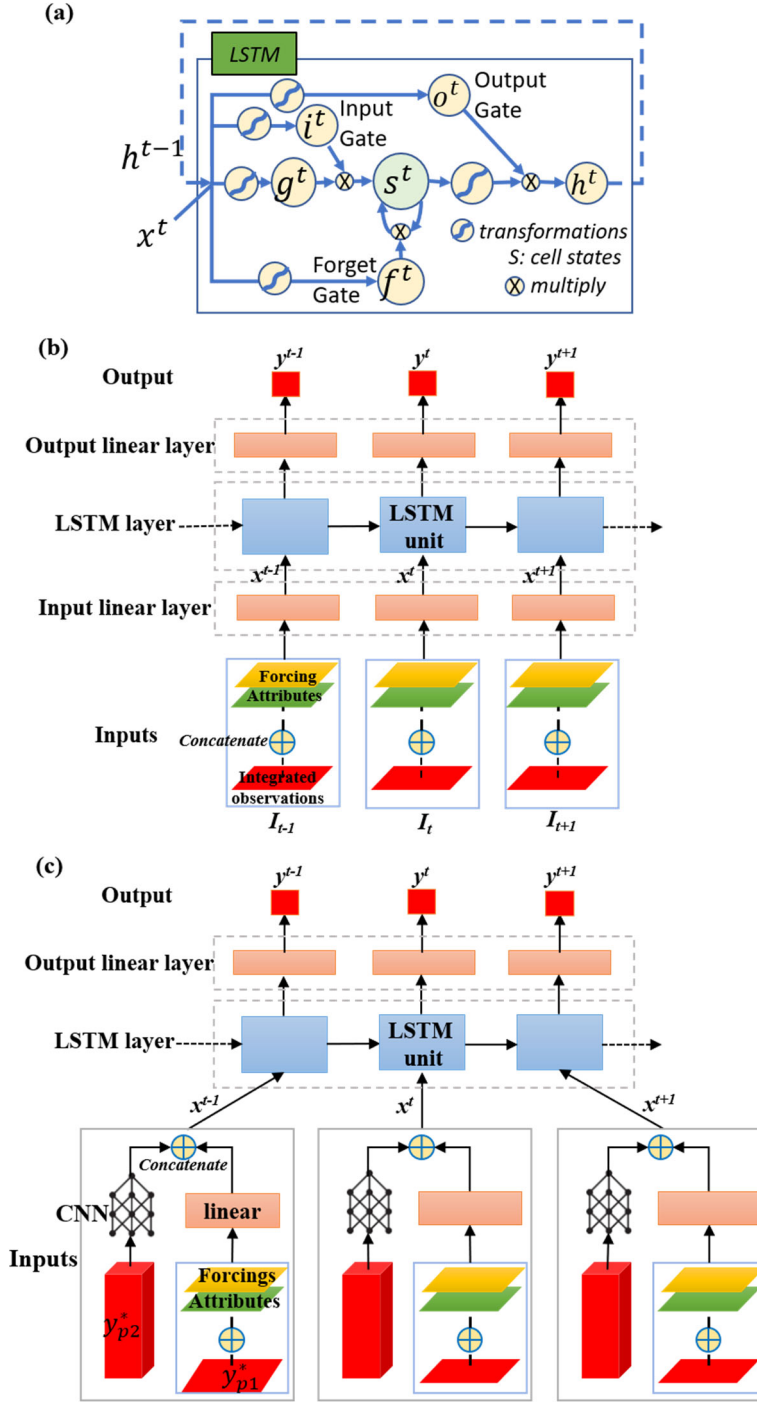


Figure 2. The illustration of the LSTM unit and the data integration (DI) method. (a) The calculation inside an LSTM unit. The dashed arrow indicates the hidden states from one time step is fed as inputs to the next time step; (b) The DI method without CNN unit, and (c) The DI method with CNN unit. Here the observation y^* is split into the directly used y_{p1}^* and y_{p2}^* , the part passing through a CNN unit. The CNN unit is optional in that if the length of y_{p2}^* is 0, e.g., in DI(1), this part of the network will not be used. For the projection model alone, neither y_{p1}^* nor y_{p2}^* would be used.

2.3. Data prep-processing

When trained on CONUS, basins from the whole dataset are batched together to calculate the loss. The batching typically assumes the errors are identically distributed. If no data preprocessing and normalization were applied, the default loss function would pay more attention to wetter and larger basins compared to drier basins. Here we tried several normalization procedures and chose the following steps which provided the optimal performance: (i) we first normalized the daily streamflow by the basin area and mean annual precipitation to get a dimensionless streamflow as the target variable, which reduced the differences between large and small basins; (ii) then, we transformed the distributions of daily streamflow and precipitation since these two typically have Gamma distributions:

$$v^* = \log_{10}(\sqrt{v} + 0.1) \quad (10)$$

where v and v^* are the variable before and after transformation, respectively. We aimed to make the transformed distributions as close to Gaussian as possible. 0.1 was added inside the log to avoid taking the log of zero; (iii) finally, we applied a standard transformation to all the inputs by subtracting the CONUS-scale mean value and then divided by the CONUS-scale standard deviation.

2.4. Reference methods

To put the performance of our proposed DI method into context, we tested reference methods including AR with exogenous inputs and a simple feedforward artificial neural network, in addition to the SAC-SMA hydrologic model provided from the CAMELS dataset. The equation of the auto-regressive model is as the following:

$$y_t = c + \epsilon_t + \sum_{i=1}^p \alpha_i y_{t-i} + \sum_{j=1}^r \beta_j x_{j,t} \quad (11)$$

Where t is the time step, y is the streamflow observations, x contains the forcing terms, p is the total order of the auto-regression model, r is the total number of forcing variables, and α_i and β_j are the estimated coefficients for the lagged streamflow observations and forcing terms, respectively. c is a constant here and ϵ_t is the white noise term. A different AR model was trained for each basin. Hence the influence of different

static attribute term for each basin is absorbed into the AR parameters. Here we trained the model with $p=1$ each basin individually and denoted the resulting model by $AR_B(1)$.

The artificial neural network used here, noted as ANN(1), is a two-hidden-layer feedforward network whose inputs include the streamflow observation on the previous day. Unlike the AR_B model, we trained one ANN model over all the CAMELS basins. The inputs to the ANN model are identical to that to DI(1), including the streamflow observations at the last time step. A typical calculation in a layer of the ANN model is:

$$S_t^k = f(W_k S_t^{k-1} + b_k) \quad (12)$$

where t is the time step, k indicates the k -th linear layer, W is the weights of linear layer, S is the output of the linear layer, b is the constant, and f is the nonlinear activation function for which we used ReLU here.

Another potential model that we could evaluate is the least absolute shrinkage and selection operator (lasso). However, comparisons in our previous work showed that ANN was a stronger model than lasso. Hence we omitted the comparison with lasso in this work. Simulation results for SAC-SMA were downloaded from the CAMELS dataset (Newman et al., 2015), and we evaluated its performance within the same test period as our LSTM model for comparison.

2.5 Evaluation metrics

The metrics used to evaluate the performance of the models include percent bias and Nash-Sutcliffe model efficiency coefficient (NSE) (Nash & Sutcliffe, 1970), all of which were calculated for each basin. We also report the percent bias of the top 2% peak flow range (FHV) and the percent bias of the bottom 30% low flow range (FLV) (Yilmaz et al., 2008). Here, considering the existence of zero flows and to be comparable with FHV, we did not calculate FLV in the log space as in Yilmaz et al., (2008). FHV and FLV highlight the performance of the model for peak flows and baseflow, respectively. All metrics are reported for the test period.

3. Results & Discussions

3.1. Performance of LSTM projection and forecast models

Without any data integration, the projection LSTM is already providing competitive predictions, while a few notable issues still exist. The median NSE of the ensemble mean of 6 projection LSTM models for the 671 basins was 0.73 (Table 2), already higher than the value (0.64) from the SAC-SMA model (Newman et al., 2015) that is commonly used in operational flood forecasting (Figure 3b and Figure 4b). SAC-SMA also had a longer calibration period of 1980-1995 and basin-by-basin calibrated parameters. CAMELS dataset include 10 different simulations of SAC-SMA and we choose the top 6 simulations that were best calibrated to calculate the ensemble metrics. For the 531 subset mentioned previously (Newman et al., 2017), the median NSE values of the ensemble mean are 0.65 and 0.74 for the SAC-SMA and projection LSTM, respectively. This comparison, consistent with the results in Kratzert et al., (2019), highlights that LSTM is a highly capable dynamics emulator and a CONUS-scale LSTM has learned the hydrologic behaviors across widely different basins without strong prior structural assumptions. We should also keep in mind that the SAC-SMA model was calibrated for each subbasin separately while one LSTM was trained for the entire CONUS. We notice that the LSTM has a good performance in Northwest (along the Rockies), in Northern California, along the Appalachian ranges and in the Atlantic states (Figure 5a) (see a map of US states in Figure A1 in Appendix A). However, the projection LSTM also has some weaknesses. The low flow component had some significant percent bias (Figure 3c and Figure 4c). 20% of the basins had a positive low flow percent bias (FLV) of 50% or more, and 8% of the basins had a negative FLV of -50% or more. Some basins even had more than 100% positive FLV. Basins where the projection LSTM gave a poor performance concentrated along the Great Plains (see a map of US physiographic province in Figure A1 in Appendix A), which extends from North Dakota to northern Texas. The other regions with relative poor performance were (i) along the southwestern border of US; (ii) northern New Mexico and southern Texas; and (iii) the plains surrounding Lake Michigan, and they will be discussed in Section 3.3.

The projection model still has room for improvement: the hyperparameters were manually tuned, and we have not carried out a systematic hyper-parameter search. The distribution transformation (Equation 10) could also be further optimized. We also did not consider factors such as the heterogeneities of topography

and land use. The authors in Kratzert et al., (2019) have reported a higher value of 0.76 for the median NSE (from 531 basins) of the 8 ensemble-averaged discharge. The remaining difference between our models and theirs could be due to the use of average climatic conditions as inputs. As explained earlier, we did not attempt to run a competition and obtain the best NSE values for the projection LSTM and, but the point is to highlight the effects of the DI and understand where and why such effects exist.

We observe ubiquitous and heterogeneous DI benefits over CONUS. The median NSE of the ensemble mean improved to 0.86 and 0.80 after integrating the one-day-lag and three-day-lag Q, respectively (Table 2), with a reduced NSE variability (**Figure 3b** and Figure 4b). For the 531 subset, these two numbers are still 0.86 (Figure 4b) and 0.80. 96% of the basins over the CONUS benefited from the data integration. The variance of bias has also been greatly reduced. To our best knowledge, a median NSE of 0.86 is the highest number reported for daily streamflow forecast for hundreds of basins spread across the US. From the map we could observe that most stations experience a modest boost of 0.1-0.2 in NSE, but there are some regions with a stronger improvement (Figure 5c). DI has strongly boosted NSE in the Great Plains from <0.4 to 0.7~0.95, except southern Texas. The largest improvements are found on the Northern Great Plains (Region A on Figure 5c, hereafter referred to as F5-A. Other regions are coded similarly), Central and Southern Great Plains (extending from south of F5-A to F5-E), Great Lakes (F5-C) and Florida (F5-G). DI has also substantially elevated NSE from 0.5~0.7 to 0.9 for the mid-latitude western states (F5-D), improving upon the already high NSE there. Everywhere else, DI was able to improve the NSE by 0.1-0.2, and sporadically 0.05 (Figure 5b-c).

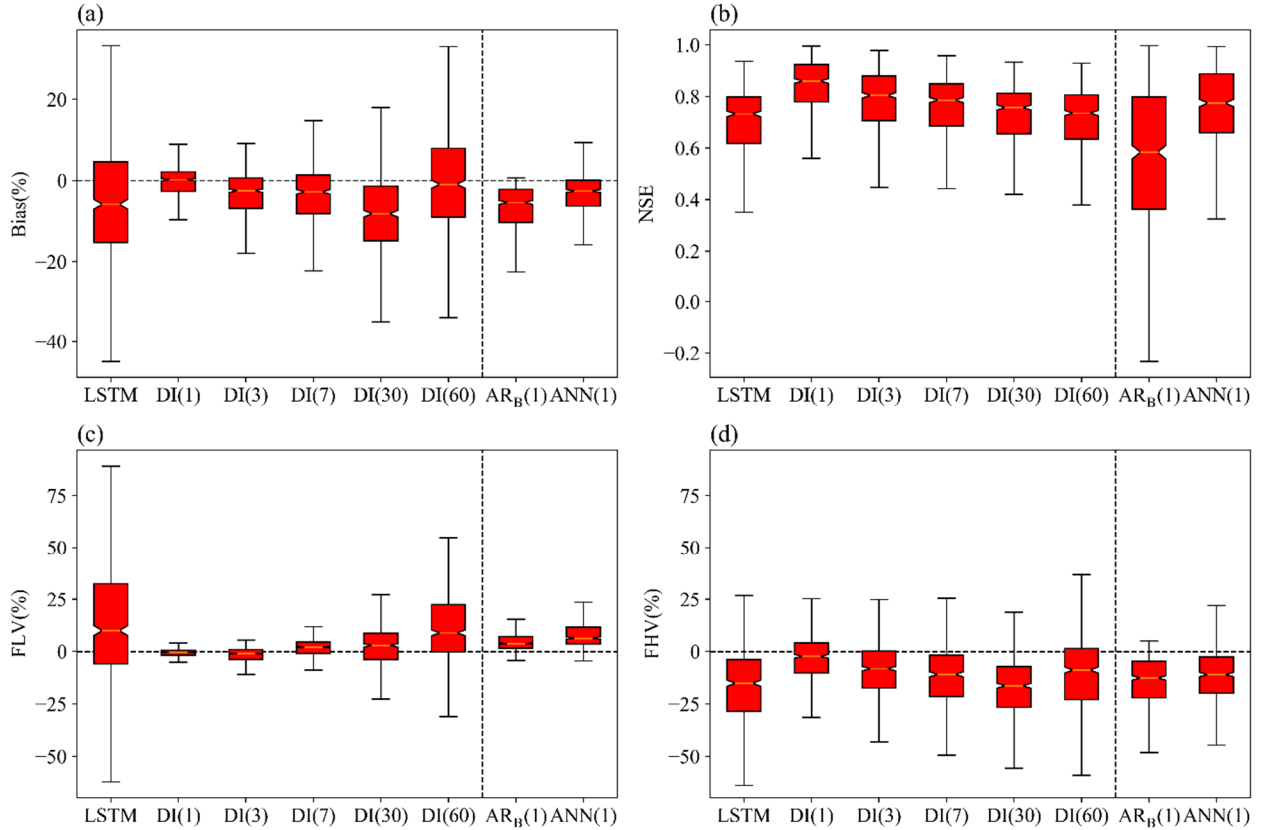


Figure 3. The performance of the projection LSTM and DI(N) models in comparison with the AR_B and ANN(1) models. DI(1) is an LSTM model that assimilates one-day lagged observation. All the metrics are calculated based on the ensemble mean discharge with six ensemble members.

DI has larger benefits on a relative basis for the low-flow regime than for high-flow regime (Figure 3c-d, Figure 4c-d). The projection LSTM could incur large bias for some stations and for ~22% of the basins, the FLV exceeded $\pm 50\%$. The projection LSTM's bias with FLV was most likely due to the lack of subsurface characteristics (geologic layering, transmissivities, and topography, etc). The bias was mostly gone with DI(1). The compaction of FHV due to DI, although still apparent, was not as significant as that of the FLV. This reduced effect is because peaks have shorter time scales and are less dependent on memory compared to low flows. Nevertheless, the DI benefits were still noticeable on FHV, representing the effects of antecedent conditions on flooding.

LSTM with DI exhibited substantial advantages over conventional statistical approaches including basin-specific AR_B(1) and CONUS-scale ANN(1) (the two boxes to the right in all panels of Figure 3), both of

which also integrate previous day's observations. $AR_B(1)$ and $ANN(1)$ can forecast with a median NSE of 0.58 and 0.77, respectively (Table 2). $AR_B(1)$ had a very small positive bias for FLV and a larger negative bias for FHV. When trained basin-by-basin, it did well with the low flows, because it is well-suited to capture recession curves. However, $AR_B(1)$ had difficulty describing fast changes. Compared to the LSTM, $AR_B(1)$ lacks the long-term memory that is needed to keep track of subsurface or snow water storages, which promote sudden snowmelt peaks or saturated excess runoff. It tends to under-estimate the peaks, even with the integration of last days' discharge. In contrast to AR_B , $ANN(1)$ had a larger positive bias for FLV and a smaller negative FHV (**Figure 3c-d**), but when lumping all flow regimes together, it tended to have an overall negative bias (**Figure 3a**). The ANN was trained to minimize the overall sum of squared error and was attempting to balance between low flows and high flows, producing a positive FLV and a negative FHV. The ANN had even a shorter memory than AR and was likely overfitted to the peaks to keep the overall NSE down.

A CONUS-scale $AR(1)$ model has also been trained, but the results were worse than the basin-by-basin $AR_B(1)$ model (Table 2). AR lacked the complexity needed to learn from a large dataset and diverse responses observed over CONUS. The AR_B models with more regressor terms, e.g., $AR_B(365)$, also did not produce substantially different results, which suggests the formulation of LSTM, rather than the number of memory storage units, is the primary difference between LSTM and AR. We also notice that ensemble averaging greatly improved performance for the $ANN(1)$, while the effects are more muted for the LSTM DI models, but $ANN(1)$ was still much inferior to $DI(1)$.

The benefit of $DI(N)$ decayed gradually with increasing N , and the box for bias gradually widened (Figure 3a). Recall that this model used single-day observations from N days ago and for each N the model was trained separately. The information provided by the observations about the near future wanes at larger lags. This gradual decay of DI benefits, to a certain extent, reflects the memory length of the hydrological processes. When integrating the daily observation one month ago, i.e., for $DI(30)$, the negative median bias of all the basins became worse than that of the projection LSTM. However, the median NSE of $DI(30)$ was

still 0.756, higher than the projection LSTM. For FLV, the benefits of DI is clear at 30-day lag (Figure3c), presumably because recession flows have longer autocorrelation periods. On the other hand, FHV started to show a worse bias at 30 days. At a lag of about two month (60 days) or longer, the integration of lagged streamflow became detrimental to the NSE.

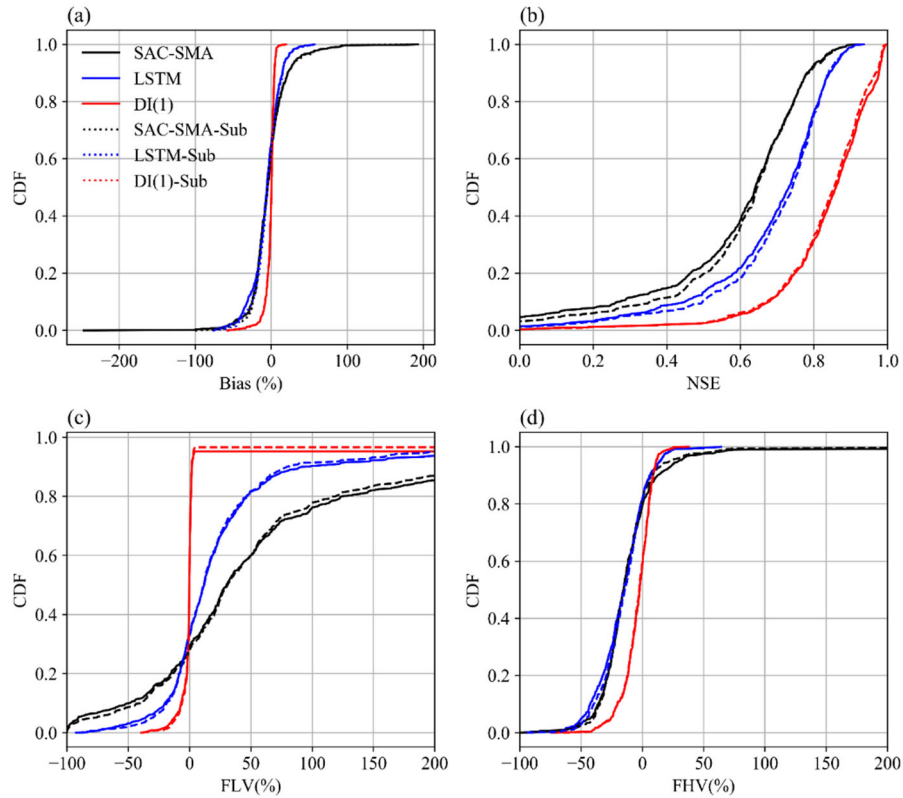


Figure 4. The comparison for the cumulative density functions (CDF) of the DL models and the SAC-SMA hydrologic model. The “-Sub” suffix refers to the 531-basin subset used in previous studies, for comparison. FLV: The percent bias of low flow regime (bottom 30%); FHV: The percent bias of high flow regime (Top 2%). The SAC-SMA model was calibrated from 1980-Oct-01 to 1995-Sep-30 and was evaluated from 1995-Oct-01 to 2005-Sep-30. LSTM and DI(1) were trained from 1985-Oct-01 to 1995-Sep-30, and the metrics were evaluated in 1995-Oct-01 to 2005-Sep-30. The CDF of FLV does not reach 1.0 because some basins have all zero flow observations for the 30% low flow interval, the percent bias can be infinite, and thus the x-axis cannot cover those basins. We set its x-axis to the same range as FHV.

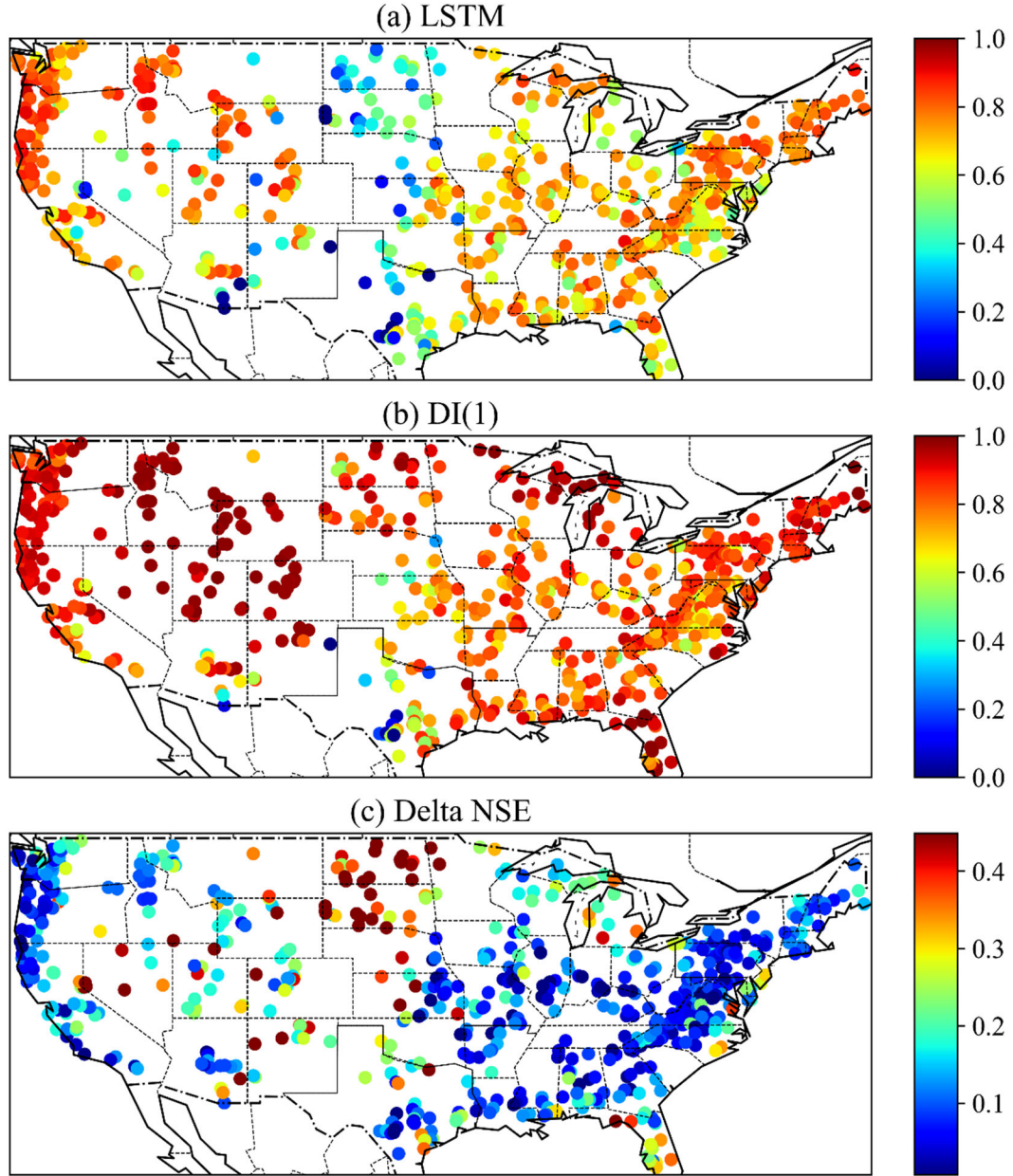


Figure 5. The comparison of NSE spatial pattern over the CONUS (a) the projection LSTM without DI; (b) DI(1); (c) $\Delta NSE = NSE_{DI(1)} - NSE_{LSTM_projection}$. Panel c has annotated regions for easy reference in the main text, and the boundaries are not precise for the related physiographies. In the paper, we denote regions A, B on this panel as F5-A, F5-B, etc.

Here we showcase several examples with large performance differences between the projection LSTM and DI(1), to visualize typical issues with the projection LSTM and how DI addressed them. Figure 6a and Figure 6b are two cases where DI significantly improved the bias with the baseflow, and their locations are marked in Figure 6h. For the basin shown in Figure 6a (in the Black Hill uplift, which is mountainous area

located inside the Great Plains, the southwest corner of F5-A), the projection LSTM materially underestimated the baseflow, was not able to reproduce the peaks either and was embarrassed by a negative NSE. However, DI(1) fixed most of the problems: DI(1) provided a strong performance in both baseflow and peaks, increasing the NSE to 0.78. For a basin in Michigan (Figure 6b), the projection LSTM has a sustained positive bias for the baseflow. Previous research suggested a major characteristic of the region is the thick glacial deposit layer inducing groundwater-dominated streamflow (Niu et al., 2014; Shen et al., 2013, 2014; Shen & Phanikumar, 2010). It is possible that no inputs were available to distinguish these hydrogeologic characteristics from other regions for the LSTM to differentially build a model for groundwater flow. DI(1) completely fixed the issue, churning out a very high NSE of 0.96. Although the projection LSTM was able to adequately describe the baseflow for a basin in the Rockies (Figure 6c), it could not reach the observed magnitudes of peak flows. DI(1) more accurately reflected both the locations and magnitudes of peaks. In a basin on the Great Plains, the projection LSTM grossly overestimated many peaks (Figure 6d). At the same time, the projection LSTM underestimated the peaks in a basin further North, in the Prairie Pothole Region (PPR, F5-B), where there is no baseflow (Figure 6f). DI(1) helped to elevate the NSE from 0.43 to 0.92 by significantly improving the peaks. We will examine the hydrologic dynamics in the Northern Great Plains (NGP) and PPR and why we find large DI gains in these regions in Section 3.3. Finally, for the point in South Texas, DI(1) did not improve the NSE. The hydrographs here show zero flow and one-day flash peaks (Figure 6g, in F5-F). This region will also be further discussed in Section 3.3.

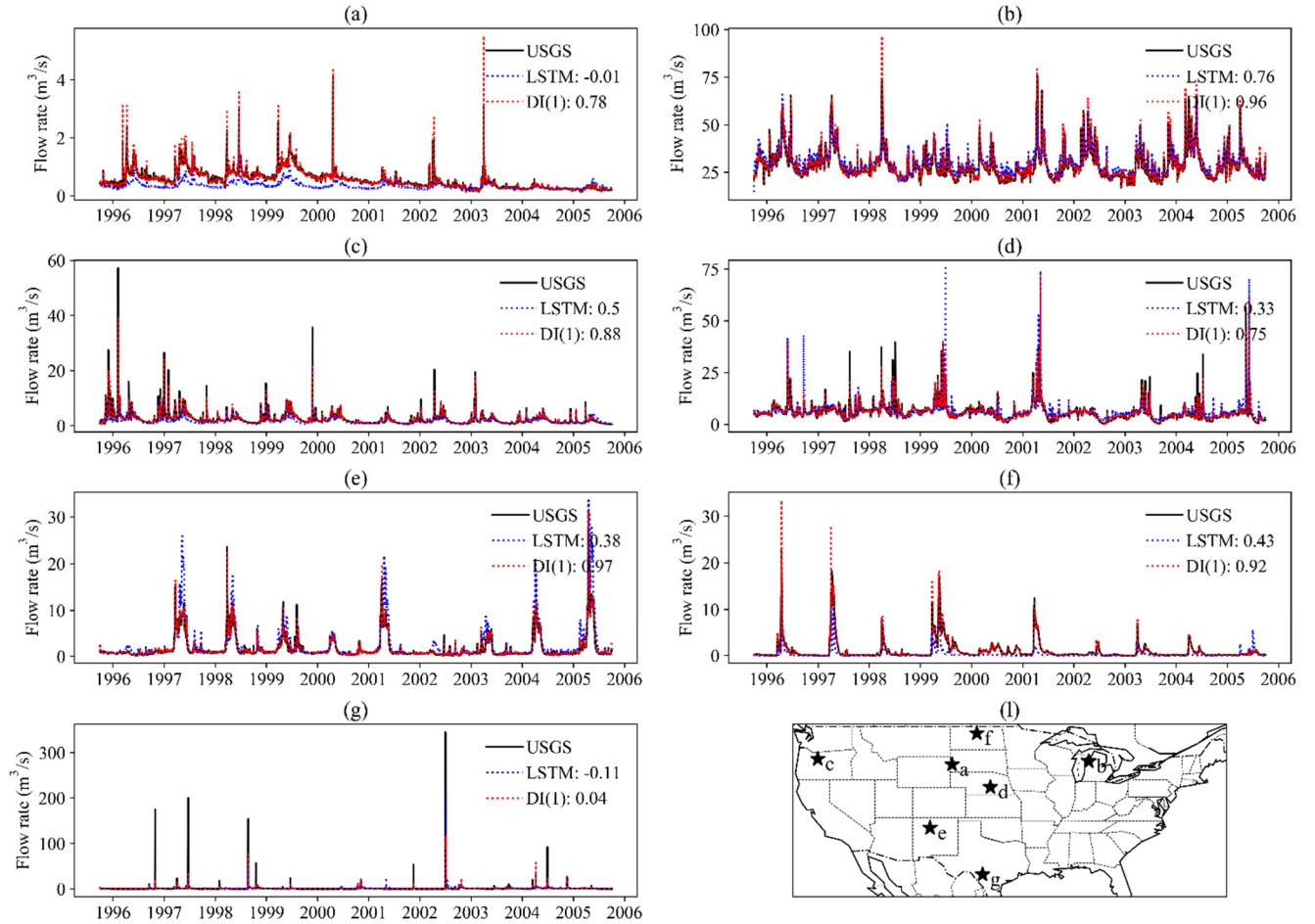


Figure 6. The time series plots of selected basins to illustrate the benefits of DI to different flow regimes. The numbers in the legends represent NSE values of the simulation.

3.2 The flexibility of the proposed DL method for integrating different forms of observations

Because of DL's special ability to automatically extract problem-relevant features and discover mathematical connections, it becomes procedurally trivial to assimilate various forms of data such as single-day, moving-averages, regularly-spaced, and multi-day measurements. These different data sources proved to all be valuable, although their effectiveness varied (Figure 7). All the DI experiments in Figure 7 improved the forecast of LSTM models except when integrating the single-day observation from one year ago (DI(365)) and the mean value of last year (DI(365)-R). If we put CNN-LSTM aside for the moment, the NSEs were in the order of $DI(N) < DI(N)\text{-R} < DI(N)\text{-M} < DI(N)\text{-A}$. In other words, providing LSTM with observations from all of the previous days is better than providing the moving averages, which is, in

turn, stronger than regularly-spaced measurements, while the least useful is data from one-day with the same lag.

Both DI(3)-A and DI(7)-A were quite close to DI(1). The gain of DI(3)-A compared to DI(1) was too small (with a mean median NSE of 0.852 vs. 0.851) (Table 2) and was not statistically significant when assessed using a two-sample student t-test. The DI(1) was even slightly higher when we used the ensemble-mean discharge. Similar to DI(3)-A, CNN-DI(1,100) also only eked out a small and statistically non-significant lead (with a mean median NSE of 0.8522) over DI(1). The DI(100)-A, in contrast, behaved noticeably worse than CNN-DI(1,100), even though they had the same information in their inputs. As expected, the DI(100)-A formulation was overfitted, while CNN-DI(1,100) was more robust. Still, consider the computational expenses required for CNN-LSTM, it can be argued that DI(1) is a better choice in this case.

There are two competing interpretations regarding the virtual equivalence of DI(1) and CNN(100)-DI(1): (i) The CNN unit did not extract any useful features from the long input series and was simply ignored by the LSTM; (ii) The CNN unit extracted useful temporal gradient features, but these features could be equally effectively extracted by LSTM via DI(1), so there is little room for improvement. Considering the detrimental impacts of DI(100)-A, it seems the CNN unit successfully carried out dimensional reduction and avoided overfitting. Hence, we are leaning toward interpretation (ii). LSTM could have learned to pass on injected observations to later time steps to construct useful features for forecast. Hence DI(1) is already a strong forecast model for this application, and it is difficult to surpass.

Table 2. The CONUS-scale median NSE values of the ensemble experiments (N=6) for different data integration and comparison scenarios

Experiment	Ensemble Statistics		Ensemble mean discharge
	Mean	Standard deviation	
SAC-SMA	0.636	0.0012	0.640
LSTM	0.714	0.0072	0.732
LSTM-Sub	0.722	0.0079	0.741
DI(1)	0.851	0.0097	0.859
DI(3)-A	0.852	0.0029	0.858
DI(100)-A	0.825	0.0088	0.840
DI(365)-A	0.785	0.0129	0.810
CNN-DI(1,100)	0.852	0.0037	0.860
CNN-DI(3,100)	0.852	0.0028	0.857
CNN-DI(1,365)	0.852	0.0039	0.860
CNN-DI(3,365)	0.850	0.0042	0.858
AR(1)	0.554	-	-
AR _B (1)	0.583	-	-
AR(365)	0.613	-	-
AR _B (365)	0.607	-	-
ANN(1)	0.650	0.020	0.774

“-Sub” means the performance on the 531 subbasins. “Mean” represents the mean median NSE of 6 ensemble runs, and “Ensemble mean” represents the median NSE of the averaged discharge from 6 runnings. All the experiments are trained from 1985-Oct-01 to 1995-Sep-30 and evaluated from 1995-Oct-01 to 2005-Sep-30.

Regularly-spaced data with coarse temporal resolution is a situation that we frequently run into, especially with satellite-based observations. Our results showed such type of data, even if at a sparse interval, offered then potential to improve forecast skill compared to the projection LSTM. However, because DI(N)-R means different distances between the observations and the day to be forecasted, it could have introduced confusion into the network, resulting in an NSE lower than that of DI(N)-M. We have attempted to include an additional input series describing the distance in time between observation and the forecast day, but it did not improve the forecast (data not shown here). Here we demonstrate the flexibility of the DL scheme to assimilate such data and show evidence of the benefit, but we think the performance of DI(N)-R can be improved with future modifications to the scheme.

Several reasons could explain the advantages of DI(N)-M over DI(N): (1) the moving average of N days has more recent information than one observation taken on the N -th past day; (2) the moving average is a more appropriate measure to represent the history of the past days than one-day measurement; and (3) potentially, the moving averages introduces less noise to the network. DI(N)-M is also better than DI(N)-R as the data is easier to interpret by LSTM. In reality, we seldom have moving average data without having the actual data from previous days, which, if available, would allow us to run the better-performing DI(1) instead. However, moving-average data would be preferred over DI(N)-R if a suitable temporal extrapolation scheme could be found, i.e., when regularly-spaced data could be re-gridded to the moving average periods. It is worth noting again here that these formulations were tested to show that these types of data could introduce benefits, but our choice will largely be constrained by what type of data is available.

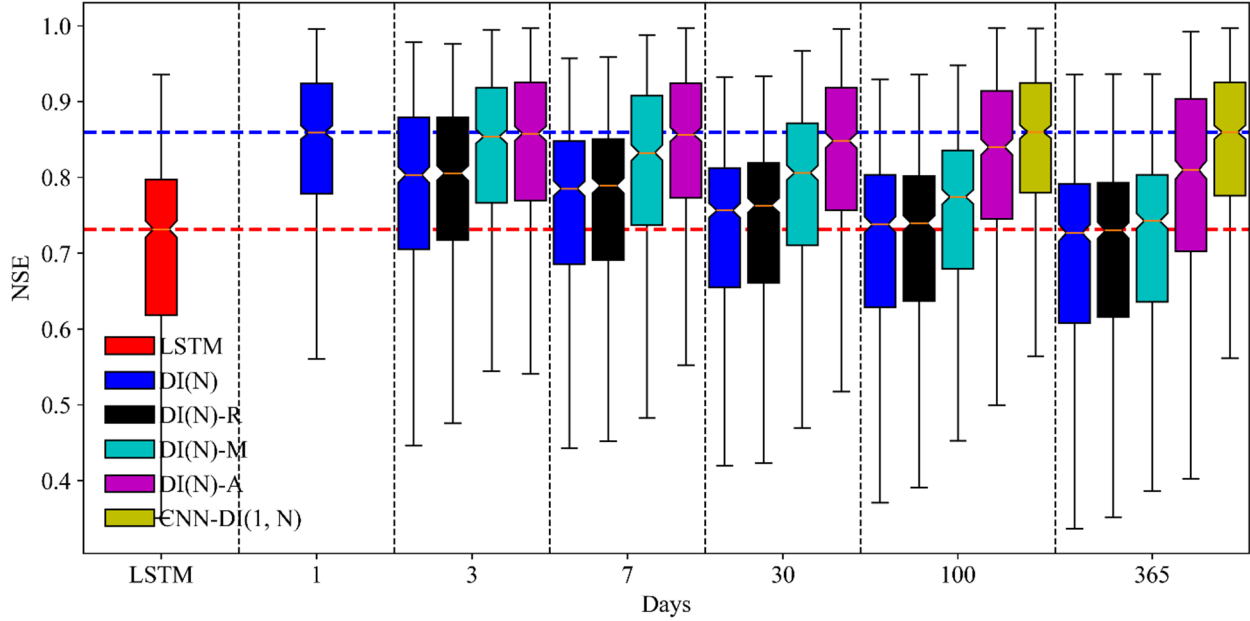


Figure 7. The comparison of different data integration experiments as a function of lagged days. The red horizontal line highlights the median value of the projection LSTM, while the blue horizontal line shows the median value of DI(1).

At least two alternative hypotheses could explain why integrating long-term-average observations are helpful compared to the projection LSTM: (i) they carry information about forcings in the distant past that was not available to the projection LSTM; (ii) they better reflect the basin storage states. We ran DI experiments where we assimilated precipitation data rather than discharge data in DI(N)-M. The benefit was minimal compared to the projection LSTM (data not shown due to its repetitive nature to the projection LSTM in Figure 7). This means that the DI benefits were not due to forcing information, and the hypothesis (i) mentioned above is not correct.

3.3. The hydrologic insights through the lens of LSTM and DI

In this section, we try to learn conditions under which the projection LSTM tended to work well or not, and where DI helped substantially or did not. The understanding here is helpful for us to anticipate the value of applying the proposed procedure. In addition, by viewing the DI benefits, we get a glimpse of the strengths of connections between sequential discharge data across CONUS and what factors control them.

3.3.1. The projection model performed better in mountainous and snow-dominated regions

From the single-factor scattered plot (Figure 8) we notice that the NSE of the projection LSTM is positively correlated with basin slope, fraction of snow and negatively correlated to soil depth, aridity, ξ and γ . Apparently, LSTM is well suited to describe snow hydrology and streamflow in mountainous basins, consistent with the results showed in Kratzert et al., (2018). LSTM could do a good job learning how to accumulate snow water in memory cells and release snowmelt water based on input forcing data (Kratzert, Herrnegger, et al., 2019). The projection LSTM also did well in regions with negative precipitation seasonality (Figure 8e), which increases basin discharge given the same amount of precipitation.

3.3.2. DI is most beneficial in regions with high streamflow autocorrelation (ACF) caused by either high groundwater contributions or connected surface water storage

Figure 8o shows correlations between NSE of the DI data points with the streamflow ACF (Figure 8o). Basins with high ACF are where we can find maximal DI benefits. This pattern could explain the strong ΔNSE with basins in NGP (F5-A) and scattered basins in Colorado, Nevada and New Mexico (F5-D). Streamflow in F5-D is contributed by groundwater as evidenced by the high Baseflow Index (Figure 1g). In the Rocky Mountains such as western Montana, Idaho, Wyoming, and western Colorado, the projection LSTM is already performing very well, with NSE mostly higher than 0.8, but DI still boosted the performance there due to large ACF. In Nevada, Utah, and northern New Mexico, where ACF is still high, but groundwater could have a very long travel time, we could also find large DI benefits.

Although high ACF often indicates large baseflow contributions and surface-groundwater connections, in some basins it does not. In the PPR (F5-B), we find basins with very little baseflow but high ACF, as shown in the example time series in Figure 6f. In the PPR, during rainfall hiatus, water contributes to the potholes (or wetlands), which are disconnected from the streams, leading to nearly zero baseflow. After heavy storms, these wetlands could establish intermittent connectivity with each other and with the streams (Leibowitz et al., 2016; Leibowitz & Vining, 2003), primarily through surface routes (Brooks et al., 2018). These intermittent connections lead to dynamical contributing areas, making it challenging for the projection LSTM to estimate flows. The wetlands serve as floodwater retention (Hubbard & Linder, 1986), introducing

a higher flow autocorrelation on a daily time scale. Hence, they lead to a large DI benefits. Besides the PPR, similar hydrologic dynamics could be found in the Upper Peninsula of Michigan (north of Lake Michigan) and Florida, although Florida has much more substantial groundwater contribution to streamflow.

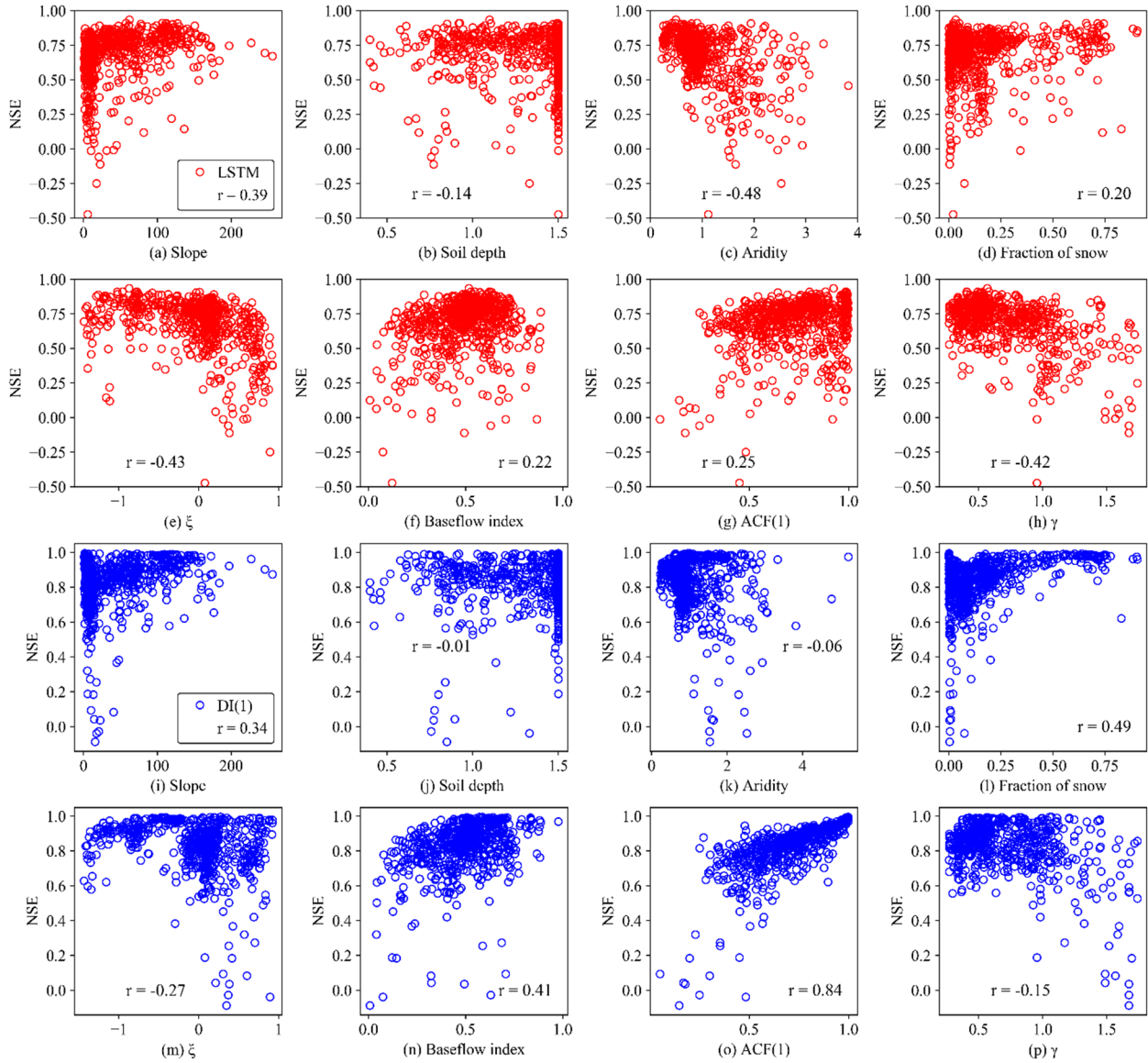


Figure 8. The correlation between NSE and basin attributes over the CONUS. The panels with red points (upper two rows) are for the projection model, and the panels with red points (lower two rows) are for DI(1). ξ : precipitation seasonality index which indicates how much precipitation and temperature are in phase; ACF(1): 1-day-lag autocorrelation function of streamflow; γ : the ratio of TWSA inter-annual and intra-annual variability.

3.3.3. Even DI cannot help with arid basins dominated by one-day flash floods

Near the US-Mexico border, i.e., southwest Texas (F5-F), southern California, southern Arizona, both the projection LSTM and the DI(1) performed very poorly. These are highly arid basins with high γ , low ACF, flashy hydrograph peaks (Figure 6g) and no storage effects. Adding to the difficulty, these flashy peaks are potentially strongly dependent on the minute-level rainfall intensity, which is not described in daily precipitation records, which could be a main reason why these peaks were poorly captured. The southwest Texas basins are also difficult to model because they are located on the karsted Edwards aquifer, which promotes fast flows and inter-basin transfers. Even DI(1) did not help here because these flash peaks are one-day phenomena and have little relationship with yesterday's discharge.

3.3.4. Precipitation seasonality, aridity and inter-basin transfers influence projection model performance but the errors could be corrected by DI.

NGP basins (F5-A) apparently caused trouble for the projection model, which is, by no coincident, consistent with previous results from conceptual models including ABCD (Martinez & Gupta, 2010) and SAC-SMA (Newman et al., 2015). There are inherent challenges in predicting streamflow in this region, although no sufficient explanations were offered. Bad performance is found from the NGP to the PPR (F5-B) in eastern North and South Dakotas. As the poor performance spreads on a diversity of landscapes, we think a general reason for such difficulty with any model is low annual basin discharge. For this semi-arid region, the precipitation seasonality that is synchronous with potential evapotranspiration (Figures 1e and 8e) increases hydrologic aridity (Berghuijs et al., 2014; Fang et al., 2016). As most precipitation arrives in the summer, when potential ET is at the maximum, it leaves little water available for runoff. For basins with small streamflow, a small bias in absolute magnitude would lead to a large drop in NSE. There could be a large number of dry days which hampered the training of LSTM. One might suspect that our normalization procedure by area and by precipitation (Section 2.3) has sacrificed these large and dry basins when training a CONUS-scale model. However, we trained a model that is normalized by long-term average discharge, but the results were very similar (Figure A2 in the Appendix). Compounding the challenge, on

the Great Plains we notice large inter-annual variability in TWSA, and the initial storage states influence streamflow. It is difficult for the projection LSTM to correctly initialize internal states related to water storages in the basin.

Nevertheless, there are also local reasons for each landscape subtype. For example, in the Black Hills and immediate adjacent subregions (southwest basins inside F5-A), the hydrogeology is highly complex (Driscoll et al., 2002): orographic precipitation induces large spatial heterogeneity in rainfall and recharge in aquifer outcrops in the mountain top. Furthermore, spring flows, sinking streams, incongruent surface and groundwater divides are common in this subregion, leading to inter-basin water transfers and frequent under-estimation of peaks. In this region, groundwater has a strong influence on the streamflow, leading to a high ACF and therefore large DI benefits. Near the center of the South Dakota-Nebraska border (southeast edge of F5-A), the rivers could also receive large groundwater contribution from the Ogallala and Sand Hills aquifers (Andrew J. Long et al., 2003) and hence large ACF and large DI benefits.

The scatter plot in Figure 9 clearly shows that basins with low NSE are mostly basins with low mean annual streamflow and high precipitation-energy synchronicity. The mid-latitude western states (F5-D) have similar annual discharge volume as the southern neighbors (in the region with $\gamma < 0.75$ and annual runoff < 200 mm/yr in Figure 9). However, they have lower γ , indicating more water passing through the subsurface system and more groundwater contribution to channels. With the high ACFs, they are all greatly enhanced via the DI. From Figure 9, it seems we can anticipate the reliability of the LSTM and DI(1) models using climatic factors and TWSA observations, although further validation is needed from other continents.

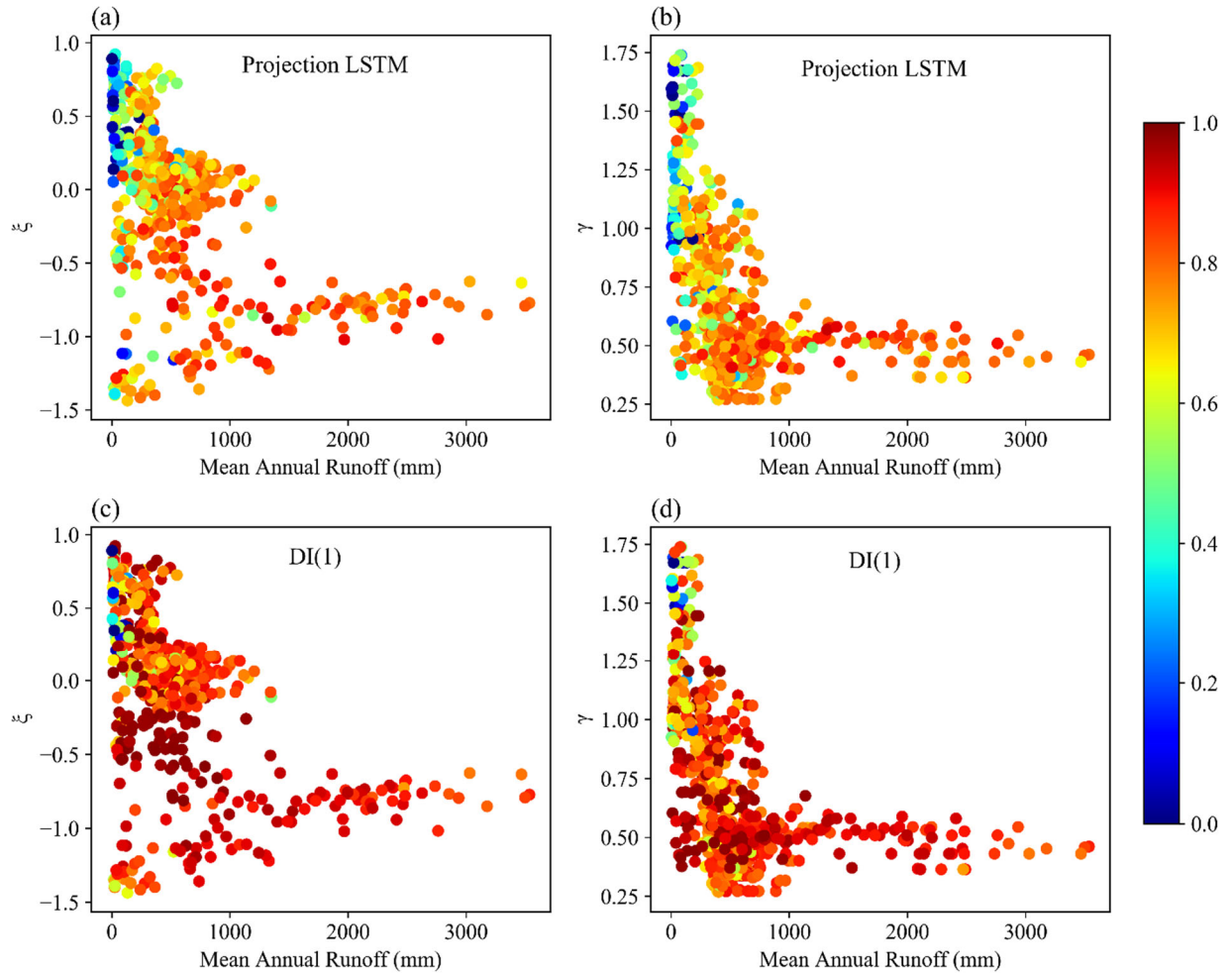


Figure 9. Scatter plots of NSE as a function of long-term mean streamflow and precipitation seasonality and inter-annual storage variability. The color in the upper and lower panels indicates NSE values for the projection LSTM and DI(1), respectively.

3.3.5. Summary

In summary, the projection LSTM has difficulty with baseflow bias and regions with low runoff volumes, strong heterogeneity, and prevalent wetlands/lakes. The latter two cases are difficult to capture by most conceptual hydrologic models as they differ from the assumptions of the standard rainfall-runoff processes. It will be difficult to improve the projection LSTM in these basins unless we provide more detailed knowledge in the inputs such as hydrogeologic inputs. However, if the streamflow has a high ACF, it can be greatly improved by integrating recent observations. High ACF could be due to either more prominent baseflow, such as the arid west or Black Hills region of the NGP, or surface water storage and intermittent

connectivity as in the PPR, in which case the peaks can also be improved. The NSE of the LSTM, with or without DI, can be low for very arid basins with one-day flashy peaks and large inter-annual TWSA variability, which alludes to less water passing through the subsurface. Analyzing these examples helps to highlight the strength and limitations of LSTM and DI. On the other hand, the behavior of LSTM also sheds insights into related hydrologic processes. For example, a large DI benefits would suggest a strong influence from slow hydrologic processes such as large groundwater and surface storages.

3.4. Further discussion and future work

There may be debates regarding whether the technique should be called data assimilation, data integration, autoregression, or other names. DI does not separately use a pre-trained forward model and also does not predict unobserved quantities. DI does achieve some primary objectives of DA, though, including utilizing recent observations to update model internal states and improve forecast. Moreover, with the same setup, it should be possible to integrate other related variables, for example, recent observations of soil moisture or canopy states, to improve streamflow forecast. Also, the LSTM has the potential to evolve into a fully functional hydrologic model and DI may evolve into many variants. These kinds of functions are far more than what conventional autoregression is typically known to offer. Thus, we think a separate term data integration is justified.

It was straightforward and uniform in integrating different forms of data with LSTM. If this were to be done with traditional data assimilation, it would have required different assimilation schemes, different covariance matrices, and varied bias correction schemes. For example, to assimilate monthly TWSA data from the GRACE, an ensemble Kalman smoothing filter algorithm needs to be applied (Reager et al., 2015; Zaitchik et al., 2008). For observations of different scales, multiscale schemes need to be employed (Pan et al., 2009). The different schemes required for different data sources and resolutions could add to the complexity of the forecast system. For the DL system, the scheme was almost uniform for all data forms, as DL would handle the mathematical details. This simplicity amounts to the liberation of human minds from certain mathematical details to focus on questioning, problem formulation, and data collection. The

flexible scheme also opens up new possibilities, including assimilating multi-day observations at the same time.

The CNN-LSTM did not produce any DI benefits compared to the simple DI(1) in this case, as DI(1) is already very strong, and we think LSTM is able to pass observations in multiple steps to construct gradient-like features. However, we could envision future scenarios where CNN-LSTM has value, as it has been shown to reduce overfitting when there are a substantial amount of raw data that could not be directly passed into LSTM. For example, the influence of topography could be introduced this way.

The current scheme does not consider the uncertainty of the observations. For example, measurement uncertainty should be higher under extreme peak flow conditions. Typical DA or data fusion schemes will incorporate such information through the update formula. Recently, we have examined how to estimate LSTM model uncertainties using newly-proposed methods and found it to have a good quality in terms of estimating predictive error, especially for temporal extrapolation (Fang et al., 2019). Hence, in the future, it should be possible to add this estimate into the data integration scheme. Moreover, in that work, we also explored having LSTM build an error model to estimate the error based on available inputs. Indeed, our analysis in Section 3.3 suggests the errors are dependent on many input attributes, and these relationships could be utilized by LSTM to build error models. Nevertheless, systematic error with the observations cannot be assessed by this method or any other data-driven method.

It can be said that the proposed DI scheme learns both the streamflow generation process and the procedure of using observations to improve forecast. We could already obtain hydrologic insights by examining the performance of projection LSTM and DI. However, it remains challenging to understand what LSTM has extracted or computed. Effort in interpretive machine learning is encouraged to shed light to the mechanisms of the LSTM updates, e.g., regarding how multi-day data are employed by CNN-LSTM and how LSTM derived its own snow storage and melt mechanisms, which could help us design better hydrologic models.

We see that the projection LSTM, while it is already higher than many operational flood prediction models at the CONUS scale, still encounters issues that seemingly could have been resolved without employing near-real-time DI. For example, for basins with significant baseflow component and inter-annual storage variability, the issue with initial states could be addressed by providing one measurement at the beginning of the simulation, baseflow conditions, e.g., monthly-average July streamflow, or even expert and non-quantitative information. Thus partial information that was difficult to utilize in a process-based model could be leveraged in DL flexibly, as long as it can be provided in sufficient quantities for training. As discussed earlier, we suspect many of the baseflow biases are due to inadequate geologic descriptions for the subsurface and would require additional input.

While DL has shown great promise here, we do not advocate it as a silver bullet that solves all problems. This work clearly showed that the projection model performed poorly on the Great Plains, just as previous conceptual models, and it clearly had limitations for the Prairie Potholes Region if no DI was applied. DL cannot create relevant information out of thin air. Nor could it distinguish between causal and associative relationships by running experiments. While our earlier work showed LSTM was able to project long-term trends in soil moisture (Fang et al., 2018), DL's capability for long-term projection for streamflow needs to be carefully evaluated. We see abundant synergies and complement between DL and process-based models (Shen et al., 2018). In the future, process-based models could be coupled to DL models, either by providing training priors, conditioning network weights, constraining loss function, etc., as outlined in Karpatne et al., (2017), to enable more reliable future projections and prediction in ungauged basins. It is generally recognized that adding physical constraints could improve the robustness of machine-learning-based predictions, an argument we are in agreement with. Although not specifically implemented in this work, we think coupling process-based model elements with DL will be among the list of future work.

4. Conclusions

In this paper, we proposed to use LSTM to integrate various types of recent streamflow observations to improve streamflow forecast performance. While the use of lagged streamflow has been demonstrated for

single-basin training data in the past, no study previously showed the effects of such forecast at continental scales or with basin attributes. Consistent with literature results, without DI, the projection LSTM is already showing results competitive with extensively-calibrated operational models, especially in mountainous and snow-dominated basins. However, like other types of hydrologic models, LSTM has issues with baseflow bias, basins with large inter-annual storage changes, hydrologically arid basins (either due to small annual precipitation or due to semi-aridity coupled to in-phase precipitation seasonality) or regions with inter-basin transfers and complex hydrogeology.

After applying the proposed DI procedure, the model was able to address most of the abovementioned issues, producing unprecedentedly high national-scale forecast NSE (0.86, from the ensemble mean discharge of DI(1)). DI provided wide-spread and spatially-varying benefits, and the largest gains were obtained for basins with strong flow autocorrelation, which suggest either strong storage-surface connections or surface water retention. Especially, model performance was greatly elevated in the Great Plains, northern Texas, Great Lakes region and semi-arid mid-latitude western states. DI can improve both baseflow and peaks for regions where peaks are induced by varying surface-water connectivity such as the Prairie Pothole Regions and Great Lakes. The LSTM with DI was substantially stronger than simpler statistical models, e.g., auto-regressive models or simpler feedforward neural networks, for both peak flow and baseflow portions of the streamflow. One region that even DI was not able to improve was southern Texas, an arid region with karst hydrogeology, flashy peaks and zero baseflow.

We found the network can flexibly integrate lagged, multi-day, moving average, and regularly-spaced time-averaged observations with a uniform structure. All of these sources of data allow the network to perform better than the projection LSTM. Such benefits were not because of the long memory of the forcings, as assimilating precipitation did not provide any gain. The flexible LSTM automatically learned how to approximate the mathematical operations for both the hydrologic process and the model-data integration procedure. This capability changes how we question and what we work on.

The more complicated CNN-LSTM architecture could not deliver statistically better performance than simply integrating 1-day-lag observations as inputs. This result is in general agreement with literature attempts where modification of the LSTM structure did not lead to performance gains. The lesson here is that, with the same sequential input information which could be utilized by LSTM, it may be difficult to design an architecture that surpasses the LSTM with significant margins.

Acknowledgments

The CAMELS dataset, including catchment attributes, forcings and streamflow, can be downloaded from the citations provided in this paper. This work was supported by National Science Foundation Award EAR-1832294. KF was partially supported by Office of Biological and Environmental Research of the U.S. Department of Energy under contract DE-SC0016605. GRACE TWSA data can be downloaded from GRACE monthly mass grids (<https://grace.jpl.nasa.gov/data/get-data/>). Streamflow data can be downloaded from U.S. Geological Survey Water Data for the Nation website (<http://dx.doi.org/10.5066/F7P55KJN>). Our LSTM code is available at GitHub (<https://github.com/mhpi/hydroDL>). We appreciate Dr. Daniel Driscoll from the USGS for conversations regarding hydrologic processes in the Dakotas.

Appendix.

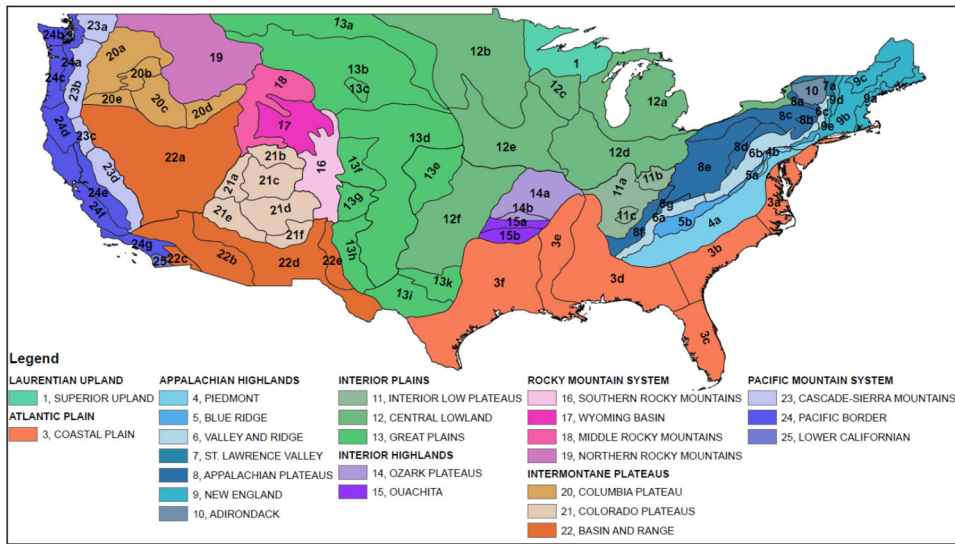
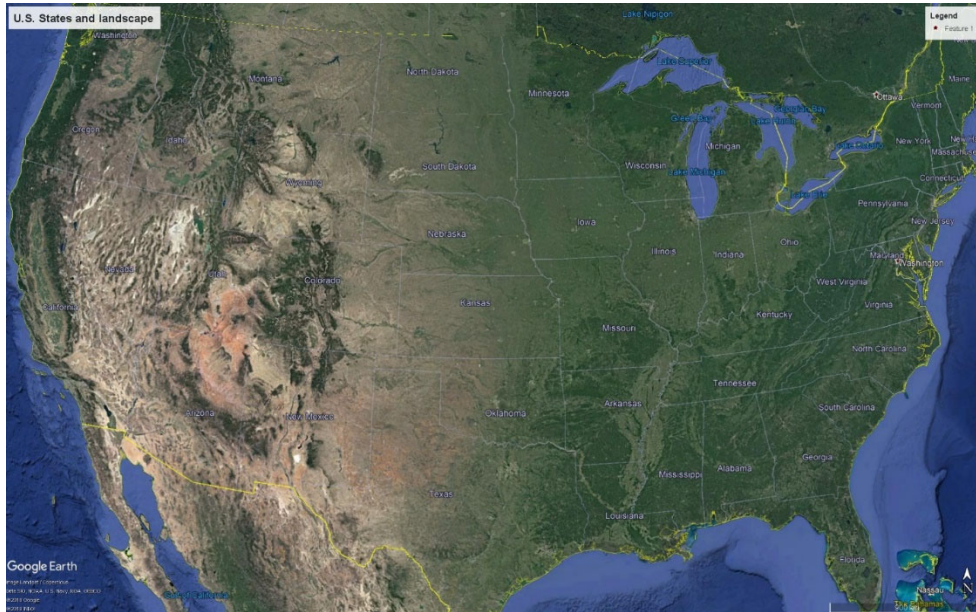


Figure A1. (a) U.S. State boundaries and landscape image from Google Earth; (b) Physiographic Provinces of the United States.

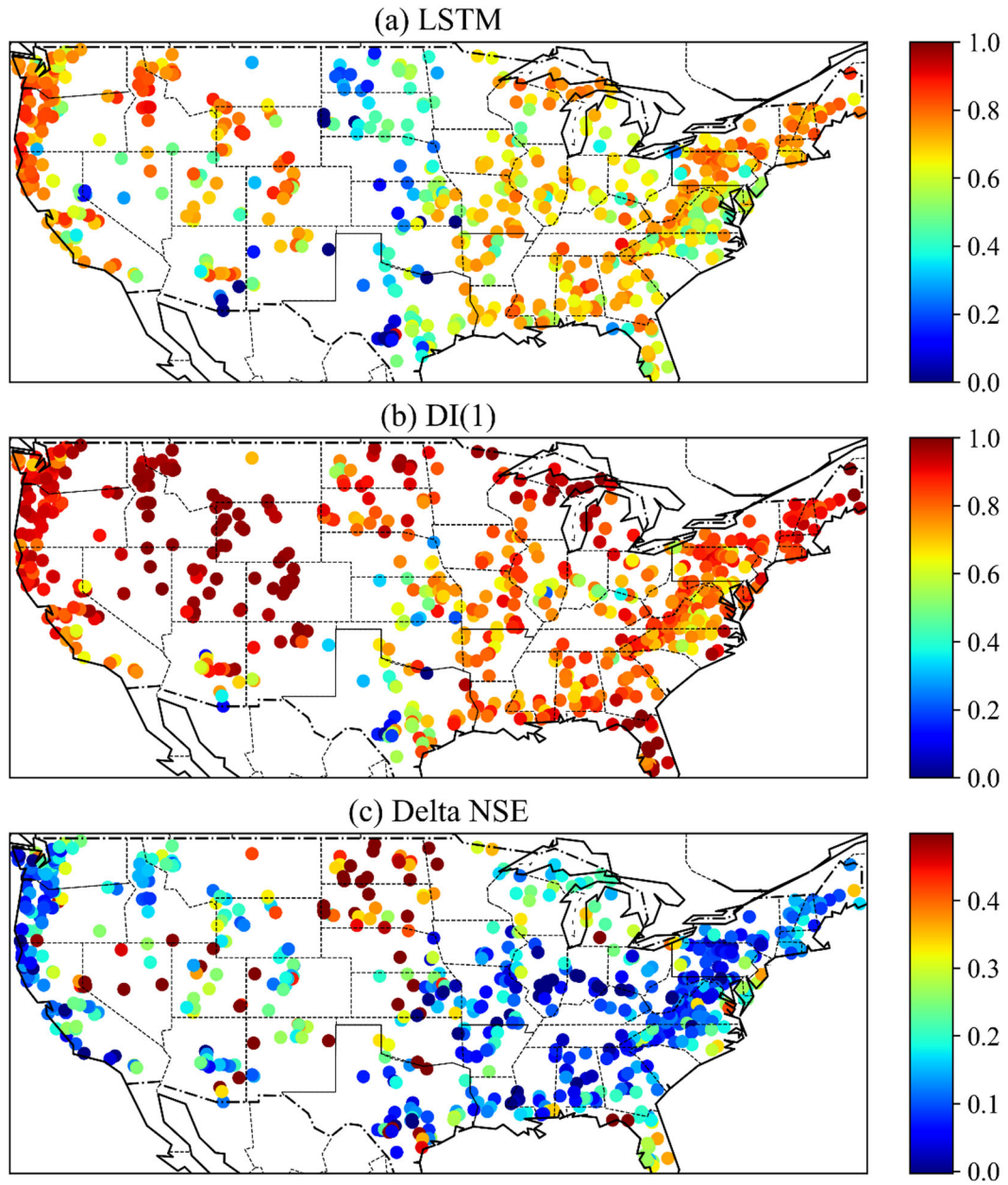


Figure A2. Same as Figure 5 but using a model with streamflow normalized by long-term average discharge for the loss calculation.

Table A1. Hyperparameters and architecture for the network

Hyperparameter	LSTM	
	Values	Values or range tested
Length of training instances	365	100, 200, 365
Mini-batching size	100	50, 100, 200
LSTM dropout rate	0.5	0, 0.2, 0.5
LSTM hidden size	256	128, 256

CNN		
Layer	Layer type	Configuration
Layer 1	Conv1d	c10k3s2/RELU/p2
Layer 2	Conv1d	c5k3s2/RELU/p2
Layer 3	Conv1d	c1k3s1/RELU/p2 for CNN-DI(1,365) c1k3s1/RELU/no-pooling for CNN-DI(1,100)

Conv1d denotes a 1D convolutional layer; c, k, s, and p are followed by the number of channels in the next layer, the kernel (or filter) size, the size of the stride, and the size of the pooling kernel, respectively. We have tuned the CNN configurations around the listed ones, but the tested configurations were numerous and are not listed here.

References

- Addor, N., Newman, A. J., Mizukami, N., & Clark, M. P. (2017). Catchment attributes for large-sample studies. Boulder, CO: UCAR/NCAR. <https://doi.org/10.5065/D6G73C3Q>
- Anderson, M. G., & McDonnell, J. J. (2005). Sacramento Soil Moisture Accounting Model (SAC-SMA). In *Encyclopedia of Hydrological Sciences*. Chichester, UK: John Wiley & Sons, Ltd. <https://doi.org/10.1002/0470848944.hsa279>
- Berghuijs, W. R., Sivapalan, M., Woods, R. A., & Savenije, H. H. G. (2014). Patterns of similarity of seasonal water balances: A window into streamflow variability over a range of time scales. *Water Resources Research*, *50*(7), 5638–5661. <https://doi.org/10.1002/2014WR015692>
- Biancamaria, S., Lettenmaier, D. P., & Pavelsky, T. M. (2016). The SWOT Mission and Its Capabilities for Land Hydrology. *Surveys in Geophysics*, *37*(2), 307–337. <https://doi.org/10.1007/s10712-015-9346-y>
- Brooks, J. R., Mushet, D. M., Vanderhoof, M. K., Leibowitz, S. G., Christensen, J. R., Neff, B. P., et al. (2018). Estimating Wetland Connectivity to Streams in the Prairie Pothole Region: An Isotopic and Remote Sensing Approach. *Water Resources Research*, *54*(2), 955–977. <https://doi.org/10.1002/2017WR021016>
- Bulygina, N., Ballard, C., McIntyre, N., O'Donnell, G., & Wheeler, H. (2012). Integrating different types of information into hydrological model parameter estimation: Application to ungauged catchments and land use scenario analysis. *Water Resources Research*, *48*(6). <https://doi.org/10.1029/2011WR011207>
- Clark, M. P., Rupp, D. E., Woods, R. A., Zheng, X., Ibbitt, R. P., Slater, A. G., et al. (2008). Hydrological data assimilation with the ensemble Kalman filter: Use of streamflow observations to update states in a distributed hydrological model. *Advances in Water Resources*, *31*(10), 1309–1324. <https://doi.org/10.1016/J.ADVWATRES.2008.06.005>

- Driscoll, D. G. (2019). *Personal communications*. Rapid City, South Dakota.
- Driscoll, D. G., Carter, J. M., Williamson, J. E., & Putnam, L. D. (2002). Hydrology of the Black Hills Area, South Dakota. Retrieved November 30, 2016, from <http://pubs.usgs.gov/wri/wri024094/>
- Entekhabi, D. (2010). The Soil Moisture Active Passive (SMAP) mission. *Proc. IEEE*, 98(5), 704–716. <https://doi.org/10.1109/JPROC.2010.2043918>
- Fang, K., Shen, C., Fisher, J. B., & Niu, J. (2016). Improving Budyko curve-based estimates of long-term water partitioning using hydrologic signatures from GRACE. *Water Resources Research*, 52(7), 5537–5554. <https://doi.org/10.1002/2016WR018748>
- Fang, K., Shen, C., Kifer, D., & Yang, X. (2017). Prolongation of SMAP to Spatio-temporally Seamless Coverage of Continental US Using a Deep Learning Neural Network. *Geophysical Research Letters*, 44, 11030–11039. <https://doi.org/10.1002/2017GL075619>
- Fang, K., Pan, M., & Shen, C. (2018). The Value of SMAP for Long-Term Soil Moisture Estimation With the Help of Deep Learning. *IEEE Transactions on Geoscience and Remote Sensing*, 1–13. <https://doi.org/10.1109/TGRS.2018.2872131>
- Fang, K., Shen, C., & Kifer, D. (2019). Separating Aleatoric and Epistemic Uncertainties of Time Series Deep Learning Models for Soil Moisture Predictions. In *ICML 2019 Workshop. Climate Change: How can AI help?* Retrieved from <https://arxiv.org/abs/1906.04595>
- Farmer, W. H., Over, T. M., & Kiang, J. E. (2018). Bias correction of simulated historical daily streamflow at ungauged locations by using independently estimated flow duration curves. *Hydrology and Earth System Sciences*, 22(11), 5741–5758. <https://doi.org/10.5194/hess-22-5741-2018>
- Ganguly, A. R., Kodra, E. A., Agrawal, A., Banerjee, A., Boriah, S., Chatterjee, S., et al. (2014). Toward enhanced understanding and projections of climate extremes using physics-guided data mining techniques. *Nonlinear Processes in Geophysics*, 21(4), 777–795. <https://doi.org/10.5194/npg-21-777->

2014

- Greff, K., Srivastava, R. K., Koutník, J., Steunebrink, B. R., & Schmidhuber, J. (2015). LSTM: A Search Space Odyssey. <http://arxiv.org/abs/1503.04069>. Retrieved from <http://arxiv.org/abs/1503.04069>
- Hirsch, R. M., & Archfield, S. A. (2015). Flood trends: Not higher but more often. *Nature Climate Change*, 5(3), 198–199. <https://doi.org/10.1038/nclimate2551>
- Hochreiter, S., & Schmidhuber, J. (1997). Long Short-Term Memory. *Neural Computation*, 9(8), 1735–1780. <https://doi.org/10.1162/neco.1997.9.8.1735>
- Houser, P. R., Shuttleworth, W. J., Famiglietti, J. S., Gupta, H. V., Syed, K. H., & Goodrich, D. C. (1998). Integration of soil moisture remote sensing and hydrologic modeling using data assimilation. *Water Resources Research*, 34(12), 3405–3420. <https://doi.org/10.1029/1998WR900001>
- Hu, C., Wu, Q., Li, H., Jian, S., Li, N., & Lou, Z. (2018). Deep Learning with a Long Short-Term Memory Networks Approach for Rainfall-Runoff Simulation. *Water*, 10(11), 1543. <https://doi.org/10.3390/w10111543>
- Hubbard, D. E., & Linder, R. L. (1986). *Spring runoff retention in prairie pothole wetlands*. *Journal of Soil and Water Conservation* (Vol. 41). [Soil Conservation Society of America]. Retrieved from <http://www.jswconline.org/content/41/2/122.short>
- Jia, X., Karpatne, A., Willard, J., Steinbach, M., Read, J., Hanson, P. C., et al. (2018). Physics Guided Recurrent Neural Networks For Modeling Dynamical Systems: Application to Monitoring Water Temperature And Quality In Lakes. In *8th International Workshop on Climate Informatics*. Retrieved from <http://arxiv.org/abs/1810.02880>
- Jia, X., Willard, J., Karpatne, A., Read, J., Zwart, J., Steinbach, M., & Kumar, V. (2019). Physics Guided RNNs for Modeling Dynamical Systems: A Case Study in Simulating Lake Temperature Profiles. In *Proceedings of the 2019 SIAM International Conference on Data Mining* (pp. 558–566). Philadelphia,

PA: Society for Industrial and Applied Mathematics. <https://doi.org/10.1137/1.9781611975673.63>

- Karpatne, A., Atluri, G., Faghmous, J. H., Steinbach, M., Banerjee, A., Ganguly, A., et al. (2017). Theory-Guided Data Science: A New Paradigm for Scientific Discovery from Data. *IEEE Transactions on Knowledge and Data Engineering*, 29(10), 2318–2331. <https://doi.org/10.1109/TKDE.2017.2720168>
- Krajewski, W. F., Ceynar, D., Demir, I., Goska, R., Kruger, A., Langel, C., et al. (2017). Real-Time Flood Forecasting and Information System for the State of Iowa. *Bulletin of the American Meteorological Society*, 98(3), 539–554. <https://doi.org/10.1175/BAMS-D-15-00243.1>
- Kratzert, F., Klotz, D., Brenner, C., Schulz, K., & Herrnegger, M. (2018). Rainfall–runoff modelling using Long Short-Term Memory (LSTM) networks. *Hydrology and Earth System Sciences*, 22(11), 6005–6022. <https://doi.org/10.5194/hess-22-6005-2018>
- Kratzert, F., Klotz, D., Shalev, G., Klambauer, G., Hochreiter, S., & Nearing, G. (2019). Benchmarking a Catchment-Aware Long Short-Term Memory Network (LSTM) for Large-Scale Hydrological Modeling. *Hydrology and Earth System Sciences Discussions*, 1–32. <https://doi.org/10.5194/hess-2019-368>
- Kratzert, F., Herrnegger, M., Klotz, D., Hochreiter, S., & Klambauer, G. (2019). NeuralHydrology - Interpreting LSTMs in Hydrology. *arXiv:1903.07903*. Retrieved from <http://arxiv.org/abs/1903.07903>
- Ladson, A. R., Brown, R., Neal, B., & Nathan, R. (2013). A standard approach to baseflow separation using the Lyne and Hollick filter. *Australian Journal of Water Resources*, 17(1), 25–34. <https://doi.org/10.7158/W12-028.2013.17.1>
- De Lannoy, G. J. M., Reichle, R. H., Houser, P. R., Pauwels, V. R. N., & Verhoest, N. E. C. (2007). Correcting for forecast bias in soil moisture assimilation with the ensemble Kalman filter. *Water Resources Research*, 43(9). <https://doi.org/10.1029/2006WR005449>

- Le, X.-H., Ho, H. V., Lee, G., Jung, S., Le, X.-H., Ho, H. V., et al. (2019). Application of Long Short-Term Memory (LSTM) Neural Network for Flood Forecasting. *Water*, *11*(7), 1387. <https://doi.org/10.3390/w11071387>
- LeCun, Y., Bengio, Y., & Hinton, G. (2015). Deep learning. *Nature*, *521*(7553), 436–444. <https://doi.org/10.1038/nature14539>
- Leibowitz, S. G., & Vining, K. C. (2003). Temporal connectivity in a prairie pothole complex. *Wetlands*, *23*(1), 13–25. [https://doi.org/10.1672/0277-5212\(2003\)023\[0013:tciaapp\]2.0.co;2](https://doi.org/10.1672/0277-5212(2003)023[0013:tciaapp]2.0.co;2)
- Leibowitz, S. G., Mushet, D. M., & Newton, W. E. (2016). Intermittent Surface Water Connectivity: Fill and Spill Vs. Fill and Merge Dynamics. *Wetlands*, *36*(S2), 323–342. <https://doi.org/10.1007/s13157-016-0830-z>
- Long, A. J., Putnam, L. D., & Carter, J. M. (2003). Simulated Ground-Water Flow in the Ogallala and Arikaree Aquifers, Rosebud Indian Reservation Area, South Dakota (WRIR 03-4043). Retrieved August 19, 2019, from <https://pubs.usgs.gov/wri/wri034043/wri034043.html>
- Maidment, D. R. (2017). Conceptual Framework for the National Flood Interoperability Experiment. *JAWRA Journal of the American Water Resources Association*, *53*(2), 245–257. <https://doi.org/10.1111/1752-1688.12474>
- Martinez, G. F., & Gupta, H. V. (2010). Toward improved identification of hydrological models: A diagnostic evaluation of the “abcd” monthly water balance model for the conterminous United States. *Water Resources Research*, *46*(8). <https://doi.org/10.1029/2009WR008294>
- Milly, P. C. D. (1994). Climate, soil water storage, and the average annual water balance. *Water Resources Research*, *30*(7), 2143–2156. <https://doi.org/10.1029/94WR00586>
- Nash, J. E., & Sutcliffe, J. V. (1970). River flow forecasting through conceptual models part I — A discussion of principles. *Journal of Hydrology*, *10*(3), 282–290. <https://doi.org/10.1016/0022->

1694(70)90255-6

- Nearing, G. S., & Gupta, H. V. (2015). The quantity and quality of information in hydrologic models. *Water Resources Research*, *51*(1), 524–538. <https://doi.org/10.1002/2014WR015895>
- Newman, A. J., Sampson, K., Clark, M. P., Bock, A., Viger, R. J., & Blodgett, D. (2014). A large-sample watershed-scale hydrometeorological dataset for the contiguous USA. Boulder. <https://doi.org/10.5065/D6MW2F4D>
- Newman, A. J., Clark, M. P., Sampson, K., Wood, A., Hay, L. E., Bock, A., et al. (2015). Development of a large-sample watershed-scale hydrometeorological data set for the contiguous USA: data set characteristics and assessment of regional variability in hydrologic model performance. *Hydrology and Earth System Sciences*, *19*(1), 209–223. <https://doi.org/10.5194/hess-19-209-2015>
- Newman, A. J., Mizukami, N., Clark, M. P., Wood, A. W., Nijssen, B., Nearing, G., et al. (2017). Benchmarking of a Physically Based Hydrologic Model. *Journal of Hydrometeorology*, *18*(8), 2215–2225. <https://doi.org/10.1175/JHM-D-16-0284.1>
- Niu, J., Shen, C., Li, S.-G., & Phanikumar, M. S. (2014). Quantifying storage changes in regional Great Lakes watersheds using a coupled subsurface-land surface process model and GRACE, MODIS products. *Water Resources Research*, *50*(9), 7359–7377. <https://doi.org/10.1002/2014WR015589>
- NOAA. (2016). Billion-Dollar Weather and Climate Disasters: Table of Events. Retrieved July 19, 2016, from <http://www.ncdc.noaa.gov/billions/events>
- NWS. (2014). Weather fatalities. National Weather Service (NWS). Retrieved July 9, 2016, from <http://www.nws.noaa.gov/om/hazstats.shtml>
- Pan, M., Wood, E. F., McLaughlin, D. B., Entekhabi, D., & Luo, L. (2009). A Multiscale Ensemble Filtering System for Hydrologic Data Assimilation. Part I: Implementation and Synthetic Experiment. *Journal of Hydrometeorology*, *10*(3), 794–806. <https://doi.org/10.1175/2009JHM1088.1>

- Reager, J. T., Thomas, A., Sproles, E., Rodell, M., Beaudoin, H., Li, B., & Famiglietti, J. (2015). Assimilation of GRACE Terrestrial Water Storage Observations into a Land Surface Model for the Assessment of Regional Flood Potential. *Remote Sensing*, 7(12), 14663–14679. <https://doi.org/10.3390/rs71114663>
- Schmidhuber, J. (2015). Deep learning in neural networks: An overview. *Neural Networks*, 61, 85–117. <https://doi.org/10.1016/j.neunet.2014.09.003>
- Shen, C. (2018). A trans-disciplinary review of deep learning research and its relevance for water resources scientists. *Water Resources Research*, 54(11), 8558–8593. <https://doi.org/10.1029/2018WR022643>
- Shen, C., & Phanikumar, M. S. (2010). A process-based, distributed hydrologic model based on a large-scale method for surface–subsurface coupling. *Advances in Water Resources*, 33(12), 1524–1541. <https://doi.org/10.1016/j.advwatres.2010.09.002>
- Shen, C., Niu, J., & Phanikumar, M. S. (2013). Evaluating controls on coupled hydrologic and vegetation dynamics in a humid continental climate watershed using a subsurface - land surface processes model. *Water Resources Research*, 49(5), 2552–2572. <https://doi.org/10.1002/wrcr.20189>
- Shen, C., Niu, J., & Fang, K. (2014). Quantifying the effects of data integration algorithms on the outcomes of a subsurface–land surface processes model. *Environmental Modelling & Software*, 59, 146–161. <https://doi.org/10.1016/j.envsoft.2014.05.006>
- Shen, C., Laloy, E., Elshorbagy, A., Albert, A., Bales, J., Chang, F.-J., et al. (2018). HESS Opinions: Incubating deep-learning-powered hydrologic science advances as a community. *Hydrology and Earth System Sciences*, 22(11), 5639–5656. <https://doi.org/10.5194/hess-22-5639-2018>
- Stocker, T. F., Qin, D., Plattner, G.-K., Alexander, L. V., Allen, S. K., Bindoff, N. L., et al. (2013). Technical summary. *Climate Change 2013: The Physical Science Basis*. Retrieved from http://www.ipcc.ch/pdf/assessment-report/ar5/wg1/WG1AR5_TS_FINAL.pdf

- Sudriani, Y., Ridwansyah, I., & A Rustini, H. (2019). Long short term memory (LSTM) recurrent neural network (RNN) for discharge level prediction and forecast in Cimandiri river, Indonesia. *IOP Conference Series: Earth and Environmental Science*, 299(1), 12037. <https://doi.org/10.1088/1755-1315/299/1/012037>
- Swenson, S. (2012). GRACE monthly land water mass grids ASCII release 5.0. Retrieved January 15, 2016, from <http://dx.doi.org/10.5067/TELND-TX005>
- Vogel, R. M., & Kroll, C. N. (1996). Estimation of baseflow recession constants. *Water Resources Management*, 10(4), 303–320. <https://doi.org/10.1007/BF00508898>
- Vrugt, J. A., Gupta, H. V., Nualláin, B., Bouten, W., Vrugt, J. A., Gupta, H. V., et al. (2006). Real-Time Data Assimilation for Operational Ensemble Streamflow Forecasting. *Journal of Hydrometeorology*, 7(3), 548–565. <https://doi.org/10.1175/JHM504.1>
- Wang, W.-C., Chau, K.-W., Cheng, C.-T., & Qiu, L. (2009). A comparison of performance of several artificial intelligence methods for forecasting monthly discharge time series. *Journal of Hydrology*, 374(3–4), 294–306. <https://doi.org/10.1016/J.JHYDROL.2009.06.019>
- Woods, R. A. (2009). Analytical model of seasonal climate impacts on snow hydrology: Continuous snowpacks. *Advances in Water Resources*, 32(10), 1465–1481. <https://doi.org/10.1016/j.advwatres.2009.06.011>
- Yilmaz, K. K., Gupta, H. V., & Wagener, T. (2008). A process-based diagnostic approach to model evaluation: Application to the NWS distributed hydrologic model. *Water Resources Research*, 44(9). <https://doi.org/10.1029/2007WR006716>
- Zaitchik, B. F., Rodell, M., & Reichle, R. H. (2008). Assimilation of GRACE Terrestrial Water Storage Data into a Land Surface Model: Results for the Mississippi River Basin. *Journal of Hydrometeorology*, 9(3), 535–548. <https://doi.org/10.1175/2007JHM951.1>

Zeiler, M. D. (2012). ADADELTA: An Adaptive Learning Rate Method. *arXiv:1212.5701*. Retrieved from <http://arxiv.org/abs/1212.5701>

Zhang, J., Zhu, Y., Zhang, X., Ye, M., & Yang, J. (2018). Developing a Long Short-Term Memory (LSTM) based model for predicting water table depth in agricultural areas. *Journal of Hydrology*, *561*, 918–929. <https://doi.org/10.1016/J.JHYDROL.2018.04.065>